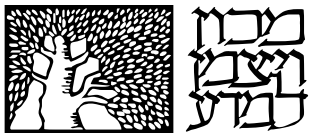

מכון ויצמן למדע
Weizmann Institute of Science

Thesis for the degree

Master of Science

חבור לשם קבלת התואר

מוסמך למדעים

By

Haim Beidenkopf

מאת

חיים ביידנקופף

Study of the Vortex Matter Equilibrium *B-T* Phase Diagram in $Bi_2Sr_2CaCu_2O_8$

מחקר דיאגרמת הפאזה *B-T* בשיווי-משקל של מערבולות הזרם ב-$Bi_2Sr_2CaCu_2O_8$

Advised by
Prof' Eli Zeldov

בהדרכת
פרופ' אלי זלדוב

December 2004

טבת תשס"ה

Submitted to the Scientific Council of the
Weizmann Institute of Science
Rehovot, Israel

מוגש למועצה המדעית של
מכון ויצמן למדע
רחובות, ישראל

Abstract

We studied the *B-T* phase diagram of the vortex matter in the layered high temperature superconductor $Bi_2Sr_2CaCu_2O_8$ using local magnetization measurements with micro Hall sensor arrays. At low temperatures we utilized the 'shaking' method, at which an in-plane *ac* field is applied to relax the vortex matter to its equilibrium state. Local *dc* magnetization measurements were taken along both field and temperature sweeps. We further probed the low temperature behavior of the vortices by combining the *ac* susceptibility technique together with the shaking method.

We found, that in addition to equilibrating the vortex matter the shaking method results also in an artificial broadening of the thermodynamic features. Nevertheless, the first order melting transition was mapped with the *dc* measurement under equilibrium conditions down to below 30 K along both field and temperature sweeps, which showed excellent agreement. The temperature sweeps resulted in particularly sharp melting steps. The melting behavior changed its character from thermally induced at elevated temperatures, to disorder-driven inverse melting behavior at lower temperatures. The entropy difference per vortex at melting, well fitted by an increasing linear behavior, changes sign with the change in slope of the melting curve. Incorporating the shaking method with the *ac* susceptibility technique recovered an equilibrium melting behavior throughout the thermally induced part of the transition down to about 40 K, below which it was replaced with a dynamic feature. Both followed closely the previously mapped melting curve.

We further mapped the first-order melting behavior in four samples with various oxygen doping levels, ranging between optimally and highly over-doped. The melting behavior indicated both a reduced anisotropy and enhanced pinning with increasing oxygen content. Overall, a more pronounced inverse melting behavior was mapped in the over-doped samples.

Preliminary results indicate on a novel phase transition, possibly of second-order. It was detected by temperature sweeps, and showed weak field dependence both above and below the first-order melting line, crossing it in close proximity to its maximum. This suggests that the *B-T* phase diagram of the vortex matter in $Bi_2Sr_2CaCu_2O_8$ actually consists of four distinct phases. Their possible nature is discussed.

Contents

Acknowledgements

I would like to thank my supervisor, Prof' Eli Zeldov, for the guidance and advice, Dr. Yuri Myasoedov for his ready assistance, and my dear colleagues Tal, Sarah, Nurit and Dima for making the past year so pleasent.

1. Introduction

The discovery of high temperature superconductivity in 1986 [1] triggered an extensive academic research. These materials belong to the subgroup of type II superconductors, that within a certain range of applied magnetic fields and temperatures allow partial penetration of magnetic flux in the quantized form of vortices.

The vortex matter in high temperature superconductors (HTSC) serves as an appealing system for the study of many-body physics. The inter-vortex repulsive interaction, that results from the magnetic moment they carry, their line tension, thermal fluctuations due to the high attainable temperatures and random underlying energy landscape, introduced by inevitable structural defects in the superconducting material, all lead to the diversity of phenomena, that can be studied in this system, and the variety of thermodynamic phases it assumes [2], which is only partially understood to date.

Experimentally the physical parameters of the vortex system can be easily tuned over a wide range of values. Its density is simply controlled by the intensity of the applied magnetic field. The underlying potential can be affected by random or correlated irradiation and vortex characteristics themselves change from one HTSC to another.

We studied the vortex matter in the layered HTSC $Bi_2Sr_2CaCu_2O_8$ (BSCCO) single crystals with a critical temperature $T_c \approx 92$ K. The vortices in this material are more susceptible to thermal fluctuations and disorder, giving rise to various phase transitions and dynamical effects, that occur at easily accessible physical conditions. In addition, the shaking method was recently shown [3] to enable the study of its low temperature glassy phases under equilibrium conditions.

Within the present research we further explored the equilibrium B-T phase diagram of the vortex matter in BSCCO, making use of the shaking method, while gaining further insight into the physics underlying the shaking method itself. The vortex state was probed through its density by local *dc* and *ac* magnetization measurements utilizing micro-Hall sensors.

This report is organized as follows. We open with a theoretical overview of superconductivity and vorticity (2). Following is a description of the various measuring techniques used in this research, and of the experimental setup (3). Next we report and discuss our findings regarding the shaking method and the B-T phase diagram of the vortex matter (4). We conclude with a brief summary of the main findings (5).

Notations

The following notations are adopted for magnetic fields and inductions:

dc components - upper case letters (e.g H_x, B_z ...).

ac components - lower case letters (e.g h_x, b_z ...).

2. Theoretical Background

2.1 Type I Superconductors

Superconductivity was discovered in 1911 by H.K. Onnes [4], who found, that below some critical temperature T_c various materials turn perfectly conducting as long as the driven current density remains below some critical value $j_\circ$. 22 years later the 'Meissner effect' was discovered by W. Meissner and R. Ochsenfeld [5], who found, that these materials show also perfect diamagnetism below a temperature dependent critical field $H_c(T) \approx H_c(0)(1-t^2)$, where $t = T/T_c$ is the normalized temperature (see Fig. 2.1). These electromagnetic properties were formulated into a set of two phenomenological equations [6], while introducing a characteristic length-scale, known as the penetration depth,

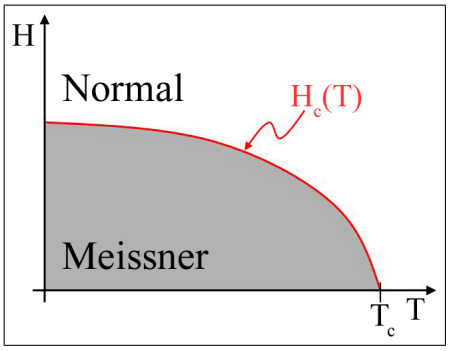

Fig. 2.1: *Schematic H-T phase diagram of a type I superconductor.*

$$\lambda = \sqrt{\frac{mc^2}{4\pi n_s e^2}} \propto (1-t)^{-1/2}, \tag{2.1}$$

with m and e being the electronic mass and charge, and n_s its density. Screening of external magnetic fields from the superconducting bulk is sustained within the Meissner state by driving shielding currents, that make the magnetic induction decay exponentially over length-scale λ from the superconductor's surface.

In 1957 Bardeen, Cooper and Schrieffer's microscopic theory [7] (BCS) specified the exact superconducting electronic ground-state, in which a condensate with a definite phase is formed, consisting of a macroscopic number of electron (Cooper) pairs, paired by a phonon mediated attractive interaction. The main electronic contribution comes from an energy band of width $K_B T_c$ around the Fermi energy, resulting in a momentum uncertainty $\Delta p \sim K_B T_c / v_F$ with v_F the Fermi velocity. Thus a second length scale, the coherence length

$$\xi \sim \frac{\hbar v_F}{K_B T_c} \propto (1-t)^{-1/2}, \tag{2.2}$$

was introduced. It gives a measure of the spatial extent of a Cooper pair, and accordingly of the condensate's rigidity against spatial variations. Together with the penetration depth it sets many fundamental properties of the superconducting material.

The condensate is protected against pair breaking excitations by an energy gap $\Delta(T)$, that vanishes at T_c. Consequently below T_c the ground-state's energy of the superconducting phase is lower than that of the normal phase by an amount, referred to as the condensation energy $E_\circ(T)$. In the presence of magnetic fields the superconducting state remains thermodynamically favorable as long as the energy, gained by condensation $E_\circ(T)$, is larger than $H^2/8\pi$, the energy invested in screening the field, as dictated by the Meissner state. Equating the two yields the critical field $H_c(T)$.

2.2 Type II Superconductors

The interplay between the two characteristic length scales, ξ and λ, divide the superconducting materials into two subgroups simply termed as type I and type II superconductors. The H-T phase diagram of type I superconductors, introduced above, consists of the homogeneous Meissner and normal phases. In the presence of magnetic fields type II superconductors exhibit also the inhomogeneous mixed (Schubnikov) phase, in which vortices - magnetic flux tubes with a normal core - penetrate the superconducting bulk, before it turns normal. The Ginzburg-Landau (GL) theory [8], unlike BCS, accounts for spatial inhomogeneities, thus suitable for modelling type II superconductivity. It was presented in 1950 as a phenomenological theory, but was rigorously derived soon after [9] as a limiting case ($T \approx T_c$) of the microscopic BCS.

2.2.1 Ginzburg-Landau Theory

Within the GL theory the superconductor's free energy functional $\mathscr{F}^{GL}$ is expanded in powers of a complex pseudo-wavefunction $\Psi(\mathbf{r})$, that serves as an order parameter, and its covariant derivative $\mathscr{D}_\mu = (\nabla + 2\pi i\mathbf{A}/\Phi_0)_\mu$, $\mu = x, y, z$

$$\mathscr{F}^{GL} = \int \mathrm{d}^3r \Big[\alpha|\Psi|^2 + \frac{\beta}{2}|\Psi|^4 + \frac{\hbar^2}{2m^*}\sum_\mu |i\mathscr{D}_\mu\Psi|^2 + f_m\Big], \qquad f_m = \frac{B^2}{8\pi} - \frac{\mathbf{B}\cdot\mathbf{H}}{4\pi}, \tag{2.3}$$

where $\Phi_0 = hc/e^* \approx 20.7$ G μm^2 is a magnetic flux quanta, e^* and m^* are the elementary charge and mass, taken to be twice those of an electron (arising from the notion of Cooper pairs), $\mathbf{A}$ is the vector potential and α, β are GL parameters, that can be expressed in terms of the length-scales ξ and λ [10]

$$\alpha = -\frac{\hbar^2\xi^{-2}}{2m}, \qquad \beta = -\frac{\alpha}{mc^2}\frac{4\pi e^{*2}}{\lambda}\lambda^3. \tag{2.4}$$

The expansion of the free energy is strictly valid close to the critical field, where both the order parameter and its derivative attain small values. Minimization of (2.3) with respect to Ψ^* and $\mathbf{A}$ yields the two GL differential equations (given in terms of a normalized order parameter $\tilde{\Psi} \equiv |\Psi| e^{i\varphi}/|\Psi_0|$)

$$\xi^2 \mathscr{D}^2 \tilde{\Psi} + \tilde{\Psi} - |\tilde{\Psi}|^2 \tilde{\Psi} = 0, \qquad \lambda^2 \nabla \times (\nabla \times \mathbf{A}) + |\tilde{\Psi}|^2 \Big(\frac{\Phi_0}{2\pi} \nabla\varphi + \mathbf{A} \Big) = 0, \tag{2.5}$$

trivially satisfied by the two homogeneous solutions $\Psi = 0$ (with $\mathbf{B} = \nabla \times \mathbf{A}$) and $\mathbf{A} = 0$ (with $|\Psi|^2 = -\alpha/\beta \equiv |\Psi_0|^2$) corresponding to the normal and Meissner phases. ξ and λ are seen (2.5) to scale the spatial variations of the order parameter and the magnetic field respectively. As a result a normal-superconducting interface can not be sharp, as full condensation and magnetic flux expulsion build over finite length. This suggests an energy balance along such interfaces with an energy cost over ξ due to loss of condensation energy, and a gain over λ due to the reduction in kinetic energy of shielding currents (both considered relative to the homogeneous superconducting state). The GL number $\kappa = \lambda/\xi$ gives a measure of the competing energies, that have to be considered in the case of inhomogeneous solutions of (2.3) and (2.5).

2.2.2 Abrikosov Vortex Lattice

In 1957 A.A. Abrikosov showed [11], that in Type II superconductors, a subfamily characterized by $\kappa > 1/\sqrt{2}$, the energy balance between gain along λ versus loss along ξ within normal-superconducting interfaces makes them energetically favorable. This suggests a partial penetration of magnetic flux in a granular fashion (as to maximize the interface volume, while minimizing the volume of the normal domain itself). The transition from the Meissner to the normal phase in such superconductors takes place gradually through the intermediate mixed phase (see Fig. 2.3). The Meissner phase is abandoned at $H_{c1}(T)$ in favor of the onset of flux penetration. The transition to the normal phase occurs at $H_{c2}(T)$, where the normal regions of the mixed phase begin to overlap.

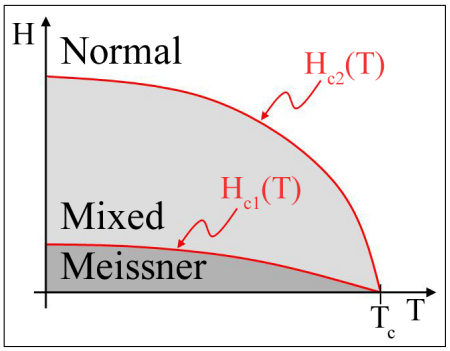

Fig. 2.2: *Schematic H-T phase diagram of a type II superconductor.*

The coherent superconducting quantum state has to be single-valued. It means, that the gained phase $\Delta\varphi$ along a flux-enclosing contour c must be a multiple of 2π

$$\frac{\Delta\varphi}{2\pi} = \frac{1}{\Phi_0} \oint_c \mathbf{A} \cdot \mathbf{dl} = \frac{\Phi}{\Phi_0} = n, \qquad n \in \mathbb{N} \tag{2.6}$$

leading to the quantization of the penetrated flux in quanta of Φ_0. The resulting picture is that of the Abrikosov vortex (AV) (see Fig. 2.3), that is a topological excitation with a normal core of radius ξ, carrying a quantum of magnetic flux with the appropriate encircling supercurrents as to produce the exponential radial decay of magnetic field over λ.

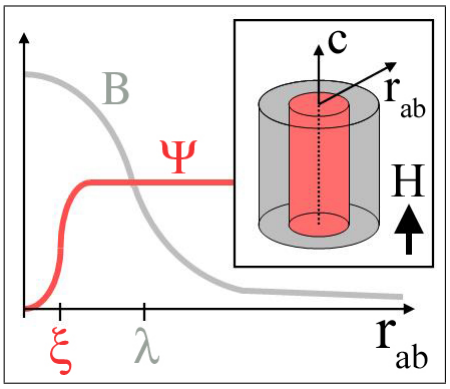

Fig. 2.3: *Structure of an AV with a normal core of radius ξ (red) and a magnetic field decaying radially over λ (gray) .*

The magnetic flux of an AV exerts a Lorentz force on the screening currents of neighboring AVs $\mathbf{F}_L = \mathbf{j} \times \mathbf{\Phi}/c$ (where $\mathbf{\Phi}$ is directed parallel to the applied field and has a magnitude of $\Phi_\circ$), giving rise to a repulsive inter-vortex interaction. Minimization of the free energy, associated with the repelling AVs (neglecting effects of finite temperatures and disorder), yields the perfectly ordered AV lattice phase, where the hexagonal lattice is shown to be the stable configuration. As apposed to the translational invariance of the system Hamiltonian the AV lattice solution possesses only a discrete translational symmetry, therefore a third length-scale is introduced

$$a_\triangle \approx \left(\frac{\Phi_0}{B}\right)^{1/2}, \tag{2.7}$$

which is just the inter vortex separation.

The AV lattice was first observed a decade after it was theoretically predicted using the Bitter decoration method [12]. This observation was followed by numerous supporting measurements, utilizing various experimental techniques such as neutron scattering [13, 14], electron microscopy [15], electron holography [16], scanning-tunnelling microscopy [17], Hall probe microscopy [18] and magneto-optics [19].

2.3 Layered Superconductors

In 1986 Bednorz and Müller discovered the first high temperature superconductor (HTSC) [1]. Although its critical temperature was 'only' 35 K, this discovery is considered revolutionary, as it was one representative of a whole family of similar ceramic oxide materials, among them BSCCO, that were found to be superconducting at elevated temperatures. Many of them remained so even well above the liquifying temperature of Nitrogen. Common to all the members of this family is a layered structure of Cu-O planes, separated by various metallic or insulating buffers, resulting in low ξ and high λ values, which make them extreme type II materials. It is mainly the Cu-O planes that are superconducting, therefore the superconducting state inherits the layered structure. These two dimensional superconducting planes are coupled to each other

by an inter-layer tunnelling of Cooper pairs, known as Josephson coupling. The layered structure introduces the distance between the superconducting planes d as a new length scale to the problem. These new features are reflected both in the theoretic models and in the observed phenomena.

2.3.1 Lawrence-Doniach Model

The Lawrence-Doniach (LD) model [20] is a discrete variant of the GL theory. It replaces all the operators, that act in the c-direction (perpendicularly to the layers) by their discrete equivalents, and allows for mass anisotropy, resulting in a phenomenological free-energy expansion

$$\mathscr{F}^{LD} = \int_{ab} \mathrm{d}^2R \Big[d \sum_n \Big(\alpha |\Psi_n|^2 + \frac{\beta}{2}|\Psi_n|^4 + \frac{\hbar^2}{2m_{ab}} |i\mathscr{D}_{ab}\Psi_n|^2 + f_c \Big) + \int \mathrm{d}z f_m \Big], \tag{2.8}$$

$$f_c = \frac{\hbar^2}{2m_c s^2} \Big| \Psi_{n+1} \exp\Big(\frac{2\pi i}{\Phi_0} \int_{nd}^{(n+1)d} \mathrm{d}z A_c \Big) - \Psi_n \Big|^2,$$

where Ψ_n is the order parameter within the n-th layer, m_{ab} and m_c are the effective masses within and perpendicular to the superconducting a-b planes respectively and f_m the magnetic free-energy density given in (2.3). Note, that f_c describes the Josephson coupling between adjacent layers.

The layered structure renders also ξ and λ anisotropic (via 2.4 with isotropic α, β)

$$\varepsilon \equiv \Big(\frac{m_{ab}}{m_c} \Big)^{1/2} = \frac{\lambda_{ab}}{\lambda_c} = \frac{\xi_c}{\xi_{ab}} \leq 1, \tag{2.9}$$

reducing the spherical symmetry to ellipsoidal, where ε gives the ratio of its main axes. This quantity takes different values for different materials, but can also be varied by changing the oxygen contents of the copper-oxide material. The oxygen concentration changes T_c non-monotonically, setting a value of optimal oxygen doping, which is the one, that maximizes the critical temperature. Anisotropy is found to decrease in BSCCO with increasing oxygen content above its optimal value (for which $\varepsilon \approx 0.01$) [21].

In the limit $\xi_c \gg d$ the discrete operators of the LD model are described well by their continuous equivalents, but the mass anisotropy is retained, resulting in the more general anisotropic Ginzburg-Landau (AGL) model

$$\mathscr{F}^{AGL} = \int \mathrm{d}^3r \Big(\alpha |\Psi|^2 + \frac{\beta}{2}|\Psi|^4 + \sum_\mu \frac{\hbar^2}{2m_\mu} |i\mathscr{D}_\mu \Psi|^2 + f_m \Big), \tag{2.10}$$

with $m_x = m_y = m_{ab}$, $m_z = m_c$.

The importance of the AGL model stretches to the study of strongly layered HTSCs with $\xi_c \lesssim d$ (such as BSCCO with $\xi_c \approx 0.2$ Å, $d \approx 15$ Å) for two main reasons. First, some of the

calculations deal with scales, that are not sensitive to the underlying discrete structure, thus the AGL model manages to capture the essentials, and produce quantitative results (an example is depicted in Fig. 2.4 and will be discussed in the next section). Second, the continuous AGL model is analytically easier to deal with than the discrete LD model, therefore it is used even in cases, where it is not strictly valid, at least to get a qualitative picture. This last point got reinforced, when it was shown, that in the limit $B \gg H_{c1}$ a simple scaling scheme can reduce the AGL expansion back to the GL one [22], yielding a scaling rule, that reproduces any anisotropic quantity from its isotropic counter part.

Anisotropy can therefore be tuned easily via oxygen doping, and accounted for theoretically using relatively simple scaling rules. Nevertheless, the layered structure comes with some new features, that anisotropy alone fails to account for.

2.3.2 Pancake & Josephson Vortex Lattices

An in-plane magnetic field penetrates a layered superconductor also in a quantized manner, known as the Josephson vortex (JV). The vortex resides in between two adjacent superconducting layers, saving the cost in condensation energy, as the order parameter in the neighboring layers is only weakly perturbed (see Fig. 2.4). The profile of the screening supercurrents, associated with the JV, follows closely the continuous anisotropic case because $\lambda_c, \lambda_{ab} \gg d$. This argument breaks on scales shorter than d and d/ε, which gives the phase core of the JV, where the currents reach their maximal value, and the phase varies nonlinearly.

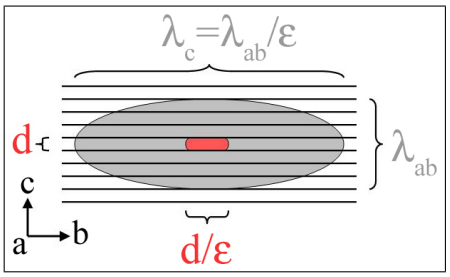

Fig. 2.4: *JV (along the a-axis) - the phase core (red) resides between two adjacent Cu-O planes. Screening currents (gray) have anisotropic profile.*

When a magnetic field is applied perpendicular to the layers the energy balance, introduced in section 2.2.2 for the case of continuous superconductors, is distributed among the individual superconducting planes, where the screening supercurrents are restricted to flow. Once penetration of a quantum of magnetic flux into a single layer becomes favorable, the flux pierces through all layers, establishing a two-dimensional pancake vortex (PV) in each one (see Fig. 2.5). The PV has the same cross-sectional structure as an AV (normal core of radius ξ_{ab} and magnetic flux decaying radially over λ_c), therefore PVs, that reside in the same layer, inherit the mutual repulsion of the AVs, whereas PVs in adjacent layers are weakly coupled by magnetic [23] and Josephson [24] interactions. The magnetic interaction is just the usual interaction between two magnetic moments. The Josephson coupling originates

from the energy, that needs to be invested in establishing a JV to redirect the magnetic flux between misaligned PVs. Both the former and the latter can be equivalently derived from minimization of f_m and f_c of Eq. 2.8 respectively. As a consequence PVs gather into aligned stacks along the c-axis to form a weakly coupled three-dimensional structure, while the repulsive interaction between the stacks leads to the formation of the PV lattice.

In highly anisotropic materials such as BSCCO stacks of PVs do not follow a tilt of the external magnetic field away from the c-axis. In these materials the coupling between the PVs is predominantly magnetic, while an in-plane field interacts with the PVs only through the Josephson coupling. Therefore, it is energetically favorable to respond independently to the c-axis and in-plane components of the tilted magnetic field [24] (up to corrections due to the weak Josephson interaction between the two), establishing the crossing-lattices configuration, in which a weakly interacting c-axis PV lattice and in-plane JV lattice coexist [25].

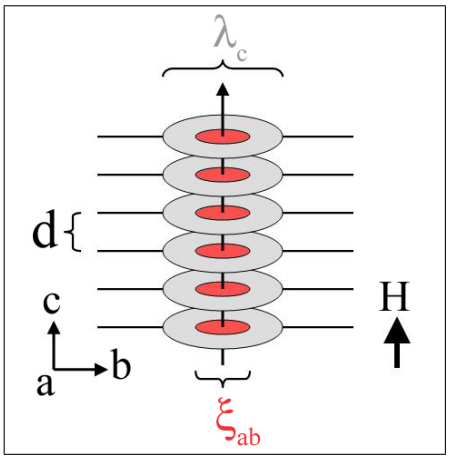

Fig. 2.5: *A stack of PVs - an individual PV has a normal core (red) and a radially decaying magnetic profile (pale gray). PVs from different layers are stacked by magnetic and Josephson coupling.*

2.4 Pancake Vortex Matter in High Temperature Superconductors

Up to this point the AV lattice and its layered variant, the PV lattice, were detached from a realistic environment. Only the elastic energy was accounted for, resulting in a perfectly ordered lattice phase, prevailing throughout the mixed state portion of the B-T phase diagram. In reality finite temperatures cause thermal fluctuations, and internal material defects establish inherent disordering potential, both challenging the perfect long-range order of the vortex lattice phase. With these two introduced each vortex must be considered a system's degree of freedom.

2.4.1 Thermodynamics

In the presence of finite temperatures the PVs fluctuate about their equilibrium lattice positions. Thermal fluctuations are naturally enhanced in HTSCs due to the high critical temperatures. In addition, the layered structure reduces the line-tension $\varepsilon_\circ = (\Phi_\circ/4\pi\lambda_{ab})^2$, softening the stacked PV structure. The high thermal energies versus low energy cost of deformation for a coherently

fluctuating segment (that is of length ξ_c) is captured by the Ginzburg number [2, 26]

$$Gi = (T_c/\varepsilon_\circ \xi_c)^2/8. \tag{2.11}$$

It characterizes the dominance of thermal fluctuations as a function of material parameters, where all quantities involved contribute to the extremely large Gi values realized in HTSCs and specifically in the highly anisotropic BSCCO ($Gi \approx 1$).

Once thermal fluctuations become comparable to the inter vortex separation, the notion of equilibrium vortex lattice positions losses its relevance, as stated in Lindemann's melting criterion

$$\langle u^2 \rangle = c_L^2 a_\triangle^2, \tag{2.12}$$

where u is the lateral distance from equilibrium, $\langle \cdots \rangle$ stands for thermal averaging and c_L is the phenomenological Lindemann constant, usually taken to be about 0.2. The PV lattice was subsequently predicted to undergo a first-order melting transition before the system turns normal [27]. The mixed state B-T phase diagram splits, accordingly, into a low temperature lattice phase, and a high temperature vortex liquid (VL) phase (see Fig. 2.6). The existence of the first-order thermal melting transition was established through various experimental measurements, among them transport [28, 29], magnetization [30, 31], *ac* susceptibility [32], calorimetric [33], neutron diffraction [34] and muon spin rotation [35].

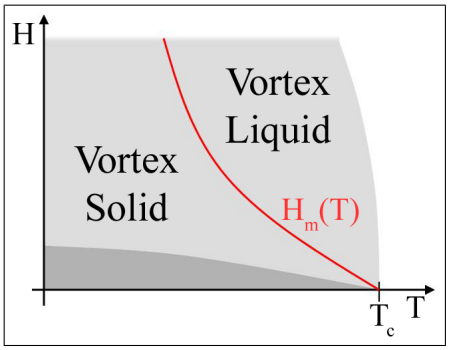

Fig. 2.6: *Schematic H-T phase diagram of clean type II superconductors. Long-range order is lost upon melting of the vortex lattice.*

In addition to the dynamic fluctuations, imposed by finite temperatures, the PV lattice is also subject to static fluctuations, caused by disorder. Disorder is brought about by inevitable structural and chemical imperfections in the underlying crystal. Superconductivity is locally weakened at the defected sites, making them energetically favorable positions for vortices. The pinning strength is usually quantified by

$$\gamma = j_c/j_\circ, \tag{2.13}$$

where j_c is the critical current density, required to unpin a vortex (via Lorentz force), and $j_\circ$ is the depairing current.

The inclusion of quenched disorder has a dramatic effect on the B-T phase diagram of the vortex matter, which is only partially understood to date. On one hand another competing energy scale is added to the accounted elastic and thermal. On the other, statistical analysis has to integrate between static fluctuations due to disorder $\overline{\langle u \rangle^2}$ and the dynamic thermal

ones $\langle u^2 \rangle$, where $\overline{\cdots}$ symbols averaging over disorder. In the former the thermal pre-averaging effectively smears the point-like disorder, hence reduces the effect of disorder at elevated temperatures, while the contribution of thermal fluctuations is naturally expected to reduce at lower temperatures [36].

Despite its reduced role at elevated temperatures, even weak disorder is still believed to destroy long-range correlations [37], turning the lattice phase more sensitive to it. Indeed it is found, that the lattice phase is replaced by a glassy one, in which vortices are slightly dislocated from their lattice sites (on a scale smaller than $a_\triangle$), quasi-long-range order is retained, and Bragg peaks are clearly detected in diffraction experiments [34], characterizing the Bragg Glass (BrG) phase [38].

Thermal melting is thus negligibly affected by the presence of disorder at relatively high temperatures [39], where quasi-long-range order is lost through a first-order transition [30]. In contrast, the low temperature behavior is dominated by disorder. Both the caging elastic potential per vortex and the pinning energy are found to decrease with increasing magnetic fields, but the former depends on it more strongly than the latter [40]. At some critical value the energy invested in distortions becomes comparable to the one gained by better adjustment to the disordered pinning potential. As a result dislocation loops proliferate, and quasi-long-range order of the BrG is destroyed in favor of an entangled vortex glass (VG) phase [41, 42, 43].

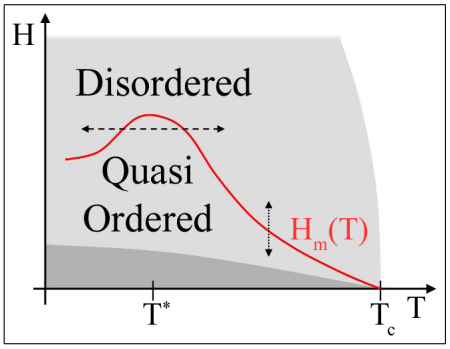

Fig. 2.7: *Schematic B-T phase diagram. Disorder included. Long-range order is lost upon melting of the vortex lattice.*

When temperature is raised within the disorder dominated region, weak thermal fluctuations about the pining centers smear the disorder potential, making it less effective in challenging the elastic forces, resulting in a rare inverse melting behavior with a negative latent heat, pushing the disorder induced melting to take place at higher vortex densities. Recent experimental work of N. Avraham *et al.* [3] indicated, that also the disorder induced transition is of first-order, merging with the high temperature thermally induced one at T^* to form a unified (non-monotonic) melting line (see Fig. 2.7), that marks the destruction of the BrG quasi-long-range correlations through a first-order transition at all temperatures [44, 45, 46, 48, 49].

The different character of the high and low temperature parts of the melting line has its implications on the high and low field phases, separated by it. While it is evident, that the low temperature VG differs from the high temperature vortex liquid, it is not clear whether they represent two distinct thermodynamic phases, or a single disordered phase, whose dy-

namic parameters change with temperature. This uncertainty may be addressed also to the low field BrG. Theory seems to lack the tools required to give an unambiguous prediction in this issue. The statistical mechanisms underlying glass transitions, although common to many physical systems, are not yet understood. Some models predict these transitions to be thermodynamic and of second-order, while other describe them as metastable dynamic states, which are separated from the stable lattice configuration by diverging energy barriers [50, 51, 52].

2.4.2 Dynamics

One of the greatest obstacles in the experimental research of the low temperature thermodynamics of the vortex matter in HTSCs is the logarithmically slow relaxation ($j_c \to 0$) processes characteristic to glasses, as vast potential barriers U_j resist flux motion $U_{j_c \to 0} \to \infty$, and separate the various metastable configurations. Consequently, at low temperatures thermal activation is incapable to trigger relaxation, and the equilibrium behavior becomes inaccessible on realistic experimental time scales. What is being measured instead, is the (very slowly relaxing, hence quasi-static) dynamic magnetization response of the sample, seen clearly in the hysteretic behavior, that opens between an upward and a downward sweeps of the applied magnetic field. The hysteretic feature closes at some temperature dependent field at which thermal and elastic energies overcome eventually the pinning potential, introducing a dynamic irreversibility line $H_{irr}(T)$ to the H-T phase diagram. As mentioned in the previous section, whether a thermodynamic transition underlies the irreversibility line or not is still an open question.

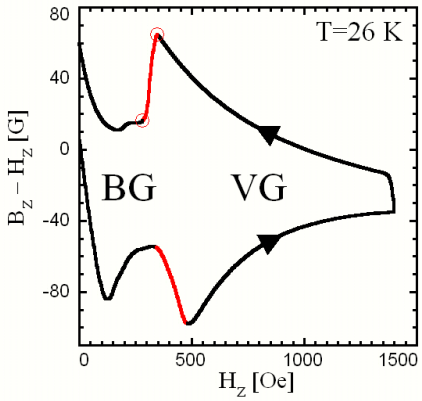

Fig. 2.8: *Hysteretic magnetization loop showing a second-peak (gray arrows), that marks an underlying transition from the quasi-ordered BrG to the amorphous VG.*

The dynamic behavior of the vortices in the presence of bulk pinning can be qualitatively understood by the Bean critical model [53], in which point pinning is averaged into a spatially uniform pinning force, again quantified by the critical current density j_c, which with the aid of Maxwell's $\nabla \times \mathbf{B} = 4\pi \mathbf{j_c}/c$ translates into a spatially uniform gradient of magnetic induction the bulk sample can sustain (instead of the magnetic induction itself being uniform as in the equilibrated case). The Bean model gives rise to a hysteretic behavior, where changes in the externally applied field can propagate into the bulk only along these critical gradients.

The onset of hysteresis at low temperatures drove the scientific research to focus on the

dynamics of the vortex matter, as the underlying phases could be probed only through their dynamic signatures. Such was the case with the extensively studied second peak phenomena (see Fig. 2.8), in which the magnetization shows a sudden increase (decrease) at a certain applied field during a upward (downward) field sweep. The phenomenon was correctly attributed [41, 46, 47, 48] to an underlying phase transition, where a better adjustment of the high field phase to disorder results in a stronger average pinning force and a higher j_c. Still, no conclusion could be inferred regarding the thermodynamic nature of the transition.

Thermodynamics is further obscured by the finite size of the superconducting samples, that adds two more sources of hysteresis. One has to do with the Bean-Livingston energy barriers the vortices face asymmetrically upon entry and exit through the sample's surface [54]. The other originates in a mismatch between the ellipsoidal symmetry of the system and its boundary conditions, as dictated by the generally nonellipsoidal sample geometry, and affects also the vortex density profile across the sample [55, 56]. The relative importance of the three hysteretic mechanisms depends on the physical conditions, such as working temperature [57] and sample geometry [58, 59].

3. Experimental

3.1 Methodology

3.1.1 Local Magnetization Measurements

The induction at the surface of a superconducting sample and its dependence on the externally controlled variables, namely temperature and magnetic field, provide valuable information regarding the state of the vortex matter. Some pronounced features can be qualitatively mapped using global magnetization measurements (for example with SQUID), that integrate over the entire volume of the sample. Such is the case with the thermodynamic first critical field and the dynamic irreversibility and second magnetization peak lines. Still, pinning and geometrical barriers (discussed in section 2.4.2) establish spatial inhomogeneities on macroscopic scales, that raise the need in detailed modelling, as to infer quantitative information regarding the vortex state from such global averages. There is even less hope with thermodynamic features, such as phase transitions, that take place at specific values of the local physical conditions, and have only faint signatures on the local vortex density.

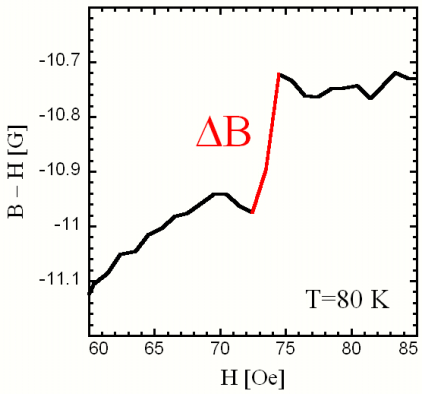

Fig. 3.1: *First-order melting transition, manifested by a discontinuous step ΔB, as seen in local magnetization measurement. The finite width of the step is due to the finite size of the Hall sensor.*

A first-order phase transition, in particular, is accompanied by a discontinuity ΔS in the system's entropy (as there is no generic reason for the entropies of the two distinct phases to be equal). According to the Clausius-Clapeyron equation it is further translated into a discontinuity in the magnetic induction (see Fig. 3.1)

$$\Delta B = -4\pi \frac{\Delta S}{\mathrm{d}H_m/\mathrm{d}T}, \tag{3.1}$$

where H_m is a temperature dependent melting field. Global magnetization measurements could not decisively identify a step at the thermal melting transition of the BrG in BSCCO [28, 31],

hence the order of the phase transition remained ambiguous.

Such a decisive identification of a first order jump can be made, only when the size of the magnetic sensor L_s gets smaller than the step's hight ΔB multiplied by the propagation rate of the melting front with increasing field $\partial r/\partial B$ (which is the inverse of the local inhomogeneity in vortex density). Estimating ΔB to be about 100mG and $\partial r/\partial B$ about 100μm/G (based on experiment) results in a critical size $L_s \lesssim 10\mu$m, characterizing local (as appose to global) magnetization measurements. This sets also the absolute sensitivity, the local sensor must support, for the detection of the melting step $\Delta\Phi < \Delta B \times L_s^2 \sim 10$ Gμm^2 $\approx \Phi_\circ/2$, which means detecting less than half a vortex, that enters on average into the active integration area of the magnetic sensor upon melting.

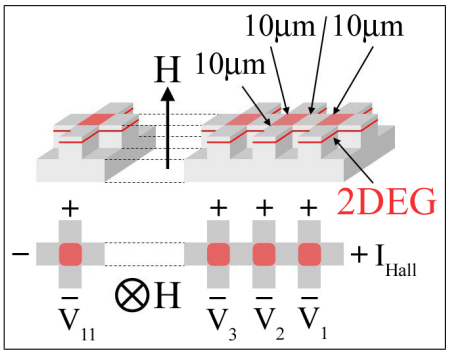

Fig. 3.2: *Schematic drawing (top: side view, bottom: upper view) of a HSA with 11 sensors, each with flux integration area (red surfaces) of size* 10×10 μm^2*, separated by* 10 μm *from each other. The 2DEG (red layer) resides* $\sim$ 1000 Å *below the HSA surface.*

Such a local micrometric magneto sensor was realized in our laboratory almost a decade ago with the two dimensional electron gas (2DEG) micro-Hall sensors (see Fig. 3.2). Its fabrication utilizes well established techniques from the field of semi-conductors. It gave way to the unambiguous identification of the first-order melting transition of the BrG phase [30]. These sensors were further concatenated into a Hall sensor array (HSA), providing spatial resolution, that allows the study of inhomogeneities and dynamic effects.

Local *dc* Magnetization Measurements

The local *dc* magnetization (*dc* magnetization) measurement is a straight forward application of the HSA. For practical reasons the B-T space is usually mapped experimentally along two distinct paths. Either the temperature or the external field are kept constant (see dotted and dashed lines in Fig. 2.7), while the other is being swept. Dynamics may show dependence on the path taken (hysteresis), but thermodynamic behavior has no such memory, and is fully dictated by the applied conditions.

The Hall sensors develop a voltage in the presence of the magnetic induction B_z at the surface of the sample (see Fig. 3.2)

$$\frac{V(H_z,T)}{I_{Hall}} = R_{Hall}\, B_z(H_z,T), \tag{3.2}$$

where I_{Hall} is the externally controlled current, driven through the sensors, and R_{Hall} is the Hall coefficient, which varies from sensor to sensor, depends on its specific realization, and has

a very small dependence on temperature and magnetic induction (i.e. non linear effects are negligible).

In strongly type II superconductors, such as BSCCO, the magnetic induction deviates appreciably from the externally applied value only close to the first critical field (once it becomes energetically favorable to let one vortex penetrate, the residual energetic cost against free vortex penetration is predominantly due to the weak elastic energy). Accordingly, eq. (3.2) is well approximated throughout most of the mixed state's B-T phase diagram by

$$\frac{V[(H_z,T) > H_{c1}(T)]}{I_{Hall}} \approx R_{Hall}\, H_z. \tag{3.3}$$

As a result the Hall coefficient can be extracted by a simple linear fit of the Hall resistivity versus applied magnetic field, and the Hall voltage, measured by the HSA, can be translated to magnetic induction. The deviation of the magnetic inductiom from the linear behavior is, in turn, exactly the physical quantity of interest, therefore data is usually presented in terms of the magnetization $4\pi M_z = B_z - H_z$ (see Fig. 3.1).

Local *ac* Susceptibility Measurements

In this study we performed also local *ac* susceptibility (*ac* susceptibility) measurements, in addition to the *dc* magnetization ones. In these measurements a small oscillatory magnetic field of amplitude h and frequency f is applied perpendicularly to the layers on top of the *dc* component H, resulting in $H(t) = H + h\sin(2\pi f\, t)$. A lock-in amplifier is used to read from the HSA both the in-phase (B') and out of phase (B'') components of the first fourier harmonic of the time dependent signal $B(t) = B(H) + b(t)$

$$B' = 2f \int_{-1/2f}^{1/2f} b(t)\sin(2\pi f\, t)\, dt, \qquad B'' = 2f \int_{-1/2f}^{1/2f} b(t)\cos(2\pi f\, t)\, dt. \tag{3.4}$$

The lock-in measurement generally improves the signal to noise ratio, and eliminates the time independent background signal.

The *dc* field H is swept in each measurement cycle at some constant temperature, while B' and B'' are measured. As long as the sweeping field is higher than $H_{irr}(T)$, the output of the measurement sweep (3.4) reduces to

$$\frac{B'(H,h)}{h} = \int \mathrm{d}\widetilde{H}\, \frac{\partial B(\widetilde{H})}{\partial \widetilde{H}}\, W_h(H - \widetilde{H}), \qquad B'' = 0, \tag{3.5}$$

which is a convolution of the derivative of the *dc* induction with the normalized window

$$W_h(\widetilde{H}) = \begin{cases} \frac{2}{\pi h}\sqrt{1 - \left(\frac{\widetilde{H}}{h}\right)^2} & ,|\widetilde{H}| < h \\ 0 & ,\text{otherwise} \end{cases} \tag{3.6}$$

of width $2h$. Consequently, this measurement is extremely useful for characterizing the non-analyticities in $B(H)$, as it directly yields the derivative of it (smeared over the probing oscillatory field h).

If the conditions $H_m(T)$ for a first-order phase transition are met along the field sweep, Eq. 3.5 results in

$$\frac{B'}{h} = 1 + \Delta B\, W_h(H_m - H), \qquad B'' = 0. \tag{3.7}$$

where ΔB is the discontinuous jump of the magnetic induction at the melting point. A first-order phase transition is therefore manifested in such a measurement (see Fig. 3.3) by the δ-like profile of the window W_h, centered around the melting field $H_m(T)$ of width twice the excitation amplitude h, and height, that is directly proportional to ΔB (and not to h).

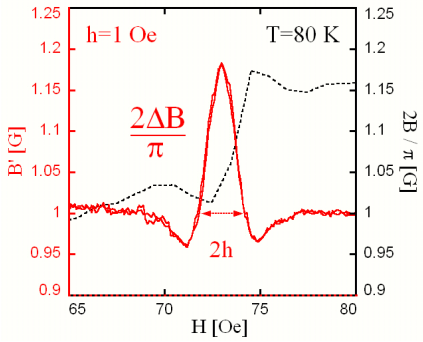

Fig. 3.3: *A first-order phase transition, manifested by a discontinuous step in a dc magnetization measurement (dashed line), is marked in an ac susceptibility measurement (red line) by a narrow peak of width* $2h$ *and height* $2\Delta B/\pi$.

Throughout the preceding discussion the vortex matter was assumed to equilibrate much faster than the period of the magnetic excitation, as is the case at high temperatures, where pinning becomes irrelevant, and the bulk vortex system follows the oscillatory component (as given by eq. 3.7). Obviously, this assumption does not hold as the irreversibility line is approached. At the other extreme the elastic energy of the vortex system is not comparable to the energy barriers, imposed either by pinning (at low temperatures) [2] or by geometrical and surface barriers (at elevated ones) [60], leading to a complete screening of the small oscillatory component $B' = 0 = B''$.

The in-phase component B' changes monotonically between those two limits - most rapidly when the balance between the hysteretic mechanisms and elasticity is close, enhancing the impact of the oscillating field. Accordingly, a dissipative off-phase component B'' appears, reaching a maximum at some intermediate field, where the energy of the oscillatory applied field is invested in surmounting the potential barriers. Hysteresis is thus manifested both by attenuation of the in-phase signal, and by the onset of the off-phase component. The thermally induced melting transition itself was found to be accompanied by an off-phase narrow peak (on top of the broad maxima) [61]. It was attributed to a small hysteresis [28], that settles mainly due to the slow relaxation processes of the BrG phase relative to the rapid ones of the liquid phase [62].

3.1.2 The Shaking Method

It has been shown, that the irreversibility line of the vortex matter shifts towards lower temperatures and fields, when a weak transverse oscillatory magnetic field is applied to it. In the presence of such a field the vortices drift towards their equilibrium configuration (on top of some induced tilt), leading to the relaxation of the off-equilibrium critical currents [63]. Willemin *et al.* employed that phenomenon in their 'shaking' method to slightly shift the irreversibility line of the vortex matter in the moderately anisotropic YBCO to lower temperatures, consequently unveiling its equilibrium melting behavior [64].

A transverse *ac* field was found to have a similar equilibrating effect on the vortex matter in highly anisotropic BSCCO samples [65], although the extreme layered structure of this material suggests an altered underlying mechanism, arising from the static crossing-lattices configuration. The transverse field penetrates and leaves the sample twice a cycle in the form of a JV lattice, while passing on its path through the c-axis PVs. When a JV crosses between two adjacent PVs, the stacked structure locally deforms [25] (see Fig. 3.4). If these PVs happen to be trapped on a point defect, the deforming force is believed to act locally to unpin them, enabling a rapid relaxation of the PV matter towards its equilibrium configuration. The shaking method may also assist the vortices in surmounting surface and geometric barriers by breaking them into smaller segments, which can then face those energy barriers and adjust to their landscape independently, again, promoting relaxation.

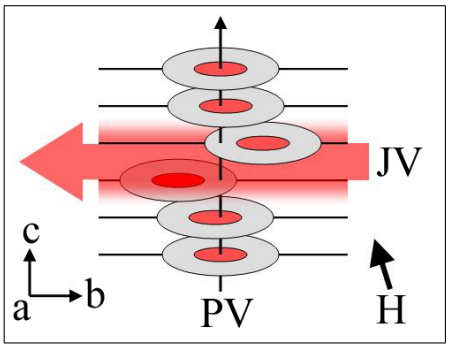

Fig. 3.4: *A JV, that crosses between two adjacent PVs, displaces them apart.*

Due to the local instantaneous nature of the JV-PV interaction, it is believed, that the shaking method does not eliminate or smear the thermodynamic effect of disorder, as an unpinned PV will be retrapped, if minimal free energy favors a pinned state. Still, caution must be retained in its application, as the oscillating JV lattice, besides catalyzing relaxation, may also introduce additional dynamics to the PV system [66], and affect its thermodynamics.

Application of the shaking method on BSCCO samples resulted in a remarkable suppression of the hysteretic behavior of the vortex matter, that gave way to a pioneering study of the low temperature vortex thermodynamics under equilibrium conditions [3]. The present research follows this path, while trying to optimize the parameters of the shaking method, and gather some additional information regarding its underlying dynamics.

3.2 Setup

3.2.1 Cryogenics & Magnetics

The cryogenic system (see Fig. 3.5) is composed of a liquid helium flow cryostat (Fig. 3.5-b) for temperature stabilization and a superconducting magnet (Fig. 3.5-d), all inside a 110 liter helium storage dewar (Fig. 3.5-c) with a 3 inch wide neck. The cryostat is a homemade double wall vessel with a needle valve (Fig. 3.5-f), enabling controlled flow of liquid helium into the sample space (Fig. 3.5-e). The walls of the cryostat are vacuum pumped before cooling it in order to achieve thermal isolation. The flow of helium is facilitated by the pressure, generated naturally within the dewar, which is maintained at about 5 psi by a pressure valve (Fig. 3.5-j). Helium leaving the system is constantly transferred via recovery lines to the helium liquefying station. The cryostat can stabilize temperatures from 4.2 K to 100 K.

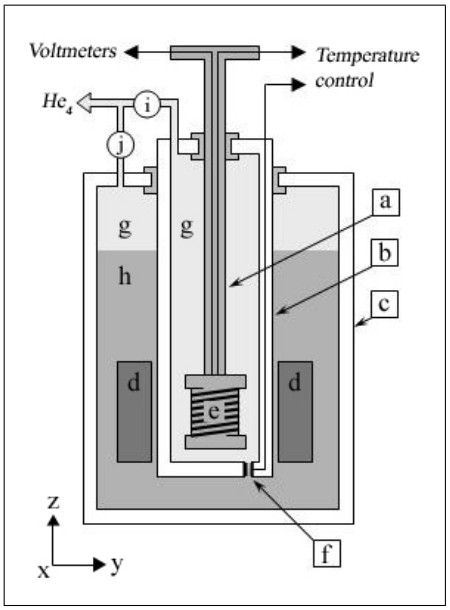

Fig. 3.5: *Schematic drawing of the cryogenic and magnetic systems. (a) rod, (b) cryostat, (c) dewar, (d) X-Z magnets, (e) sample space and heater, (f) heater and needle valve, (g) gaseous He_4, (h) liquid He_4, (i) needle valve, (j) 5 psi valve.*

Temperature stabilization is achieved by careful control of the flow and the temperature of the gas entering the sample space. The flow is controlled externally by a flow-meter (Fig. 3.5-i), and internally through the needle valve, mentioned above. The temperature is measured and stabilized using two temperature controllers both in close proximity to the sample (Fig. 3.5-e) and at a heat exchanger copper block, where the gas enters the cryostat (Fig. 3.5-f). In this way, most of the high power heating is done before the gas reaches the sample's vicinity, and only sensitive low power stabilization is done near the sample. The temperature sensors used were factory calibrated Lakeshore TG-120PL GaAs diodes. The diodes cover a 1.4 K-500 K range, have low magnetic field dependence, and require no periodic recalibration. The two 25 Ω heaters were wound from NiCu 5 mil wires. For temperature control we used Lakeshore 330 and Lakeshore 340 temperature controllers.

The external magnetic fields were applied using two separate superconducting magnets immersed in liquid helium inside the dewar. These are located at the bottom of another cylindric tube, that surrounds the lower part of the cryostat. Both produce a uniform magnetic field at the location of the sample, but in perpendicular directions, denoted in Fig. 3.5 and

hereafter by X and Z. The Z-coil has a current response of 292.8 G/A, the X-coil of 42.2 G/A.

The in-plane *ac* shaking field was generated in the X-coil. The current to it was driven by a Kepco amplifier, which in turn was modulated by an Agilent 8904a signal synthesizer. The default applied shaking field had an amplitude of 350 G and a frequency of 10 Hz, which was the highest frequency we could apply without generating excessive heat by the superconducting magnets.

Sample mounting and electrical connections to the measuring apparatus were done using a sample rod (Fig. 3.5-a). The central body of the rod is a 3/4" diameter stainless steel tube. A 24-pin socket, located at the bottom of the rod, accepts a 24-pin chip carrier, connected to the HSA on which the sample is mounted. The socket can be externally rotated about two perpendicular axes (together with the HSA and the sample), enabling the alignment of the surface of the HSA along the X-direction with an accuracy of a few milli-degrees. As a result, when a 100 Oe shaking field is applied along the X-direction and parallel to the superconducting planes of the BSCCO sample, the projection on the perpendicular Z-direction is only 10 mOe. The temperature sensor and the heater for temperature control are also at the bottom of the rod, which are covered by a protective cover. The HSA and the temperature sensors are connected to the connectors at the top of the rod using Teflon coated wires twisted in pairs to minimize pickup.

3.2.2 Hall Sensors & Sample Preparation

Most of the results, reported herein, were obtained with a slightly over-doped (SOD) BSCCO crystal ($T_c \approx 90$ K), grown using the travelling solvent floating zone method [67], that was polished into a triangular prism shape of base 660 $\times$ 270 μm^2 and height 70 μm. Three additional BSCCO samples [68] with different oxygen stoichiometries were measured. An optimally doped (OPD) ($T_c \approx 92$ K) crystal and an over-doped (OVD) ($T_c \approx 88$ K) crystal were cut into disks with diameters of 400 μm and 600 μm respectively. A highly over-doped (HOD) crystal ($T_c \approx 85$ K) was cut into a square with 230 μm sides. All of the three had thickness of about 50 μm.

The samples were mounted on the surfaces of HSAs, each with eleven sensors of 10x10 μm^2, 10 μm apart (see Fig. 3.2). The sensors were made from 2DEG, formed at a GaAs/AlGaAs interface. The 2DEG active layer resided only 1000 Å below the surface, resulting in a very accurate measurement of the local magnetic field at each of the sensor locations across the sample. The 2DEG usually has a mobility of about 1×10^5 cm^2/V sec at 80 K and a density of about 6×10^{11} cm^{-2}, resulting in a sensitivity of about 0.1 Ω/G.

We found, that a *dc* Hall current of 400 μA, driven through the array, optimizes the signal

to noise ratio. In the *dc* magnetization measurements the Hall voltage was measured using a Keithley 182 sensitive digital voltmeter for two opposite polarities of the Hall current. In the *ac* susceptibility measurements an SR 850 lock-in amplifier measured the signal from the sensors. In general the sensors were measured one after the other for each temperature and field by switching the voltmeter or lock-in connection to each sensor, using a Keithley 7001 switch system. In particularly sensitive measurements several voltmeters or lock-in amplifiers were used simultaneously, each measuring the Hall voltage of a specific sensor.

The entire experiment was controlled by a computer program written in LabView. The input from the measurement apparatus was carried through a GPIB bus (IEEE-488 standard interface).

4. Experimental Results & Discussion

The shaking method, in which the vortex matter is relaxed by an in-plane oscillatory magnetic field, was employed extensively to enable the study of the equilibrium B-T phase diagram of the vortex matter in BSCCO. For that purpose we conducted *dc* magnetization measurements, in which both field and temperature sweeps were taken. In addition we incorporated the shaking method with the *ac* susceptibility measurement. Below we report the results of applying the in-plane shaking field together with the different measuring techniques, and the implications they bare on the physics underlying the method. We present the emerging thermodynamics of the vortex matter. Next, we present the measurements taken with four different BSCCO samples, each with a different Oxygen doping level, which is known to alter the material's anisotropy. We conclude with a report of a possible novel phase transition.

4.1 Equilibration by the Shaking Method

We start by revisiting the effect an in-plane oscillatory magnetic field has on the c-axis vortex matter, as seen with *dc* magnetization measurements along a field sweep. As was reported before by N. Avraham [3], the onset of hysteretic profiles is suppressed to much lower fields and temperatures on application of the shaking method with BSCCO samples. The thermodynamic properties of the vortex matter, previously obscured by dynamic effects, can then be studied within the extended reversible regime. As temperature is further lowered, irreversibility reappears, marking a generalized irreversibility line $H_{irr}^{h_x}(T)$, below which the thermodynamic behavior is still obscured, even in the presence of a shaking field of amplitude h_x.

The experimental setup enabled us to apply higher *ac* in-plane fields than before (usually up to 350 Oe). As a result the intersection point of the inverse melting line with $H_{irr}^{350}(T)$ shifted below the temperature of 30 K with all studied samples. Fig. 4.1 shows the results of field swept *dc* magnetization loops taken with the OPD sample. At 29.5 K (Fig. 4.1-a) a shaking amplitude of 350 Oe indeed suppressed the hysteretic behavior to fields lower than the melting one. Consequently, the second-peak feature (blue line) collapsed into a thermodynamic melting step (red line). On the other hand at 28.5 K (Fig. 4.1-b) the same shaking field failed to do so,

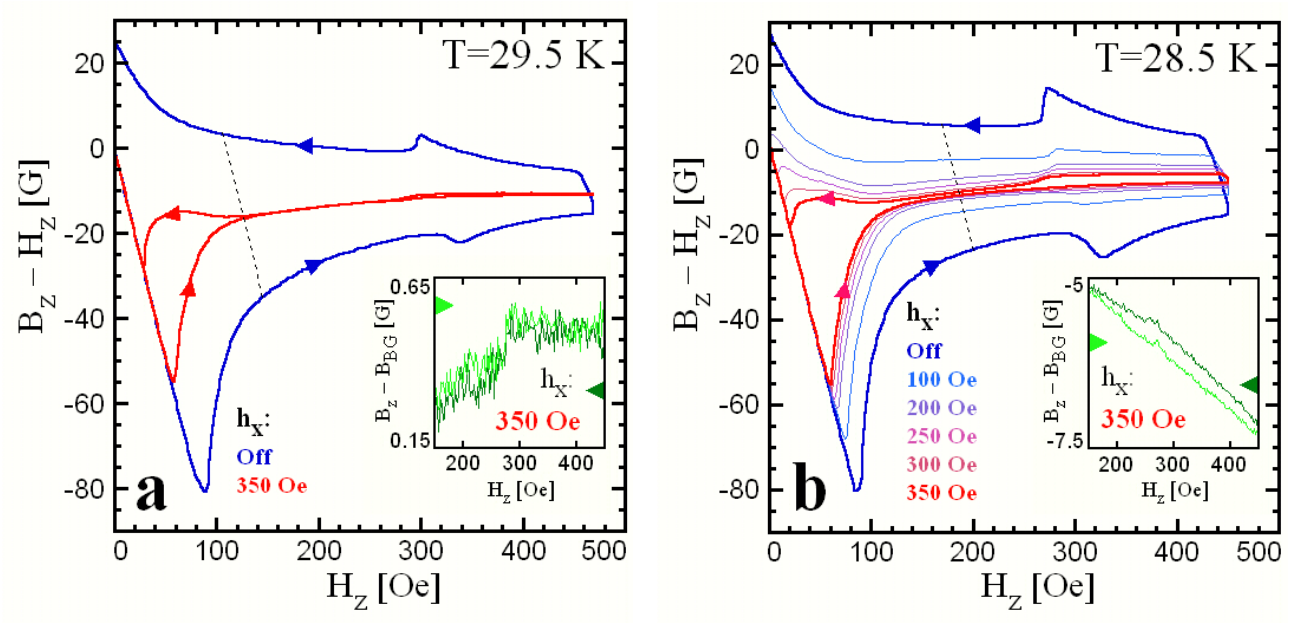

Fig. 4.1: *(**a**) Hysteretic magnetization loop taken at 29.5 K showing a fully developed second-peak (blue line) versus a partially relaxed loop (red line) revealing an equilibrium melting step. (**b**) At 28.5 K the magnetization loops remain hysteretic at all applied shaking fields. Insets: local magnetization technique is used to eliminate the background signal (measured by a neighboring sensor). Shows reversibility between sweep up (pale green line) and down (dark green line) at 29.5 K, and irreversibility at 28.5 K.*

setting the intersection point to take place about 29 K for this sample.

To better quantify the effect of shaking on the hysteretic behavior, we measured magnetization loops, while applying different shaking amplitudes at various temperatures (given in Fig. 4.1-b for 28.5 K). We then extracted the variation of the magnetization at the onset point of irreversibility in the presence of a 350 Oe shaking field $M_z(B_{irr}^{350}, T)$, as the shaking amplitude is reduced down to zero (along the dashed lines in Fig.s 4.1-a,b). The results are gathered in Fig. 4.2-a. The suppression of hysteresis as a function of shaking amplitude seems to be fitted quite well (up to fields of about 250 Oe) by a decaying exponential behavior with a characteristic field of about 100 Oe.

Besides assisting relaxation strong shaking fields might alter the equilibrium properties of the PV matter itself. The same short-range JV-PV attractive interaction, which is believed to produce the agitation of the PVs in the shaking method, reduces the energy cost, associated with each PV. As a result the PV matter is slightly denser in the presence of a crossing JV [69] (an induced density wave is thus an equivalent way of describing the shaking method). Consequently the PV matter melts already at lower applied fields, when a *dc* in-plane field H_x is present (see Fig. 4.2-b). This shift is linear in the magnitude of the in-plane field [25]

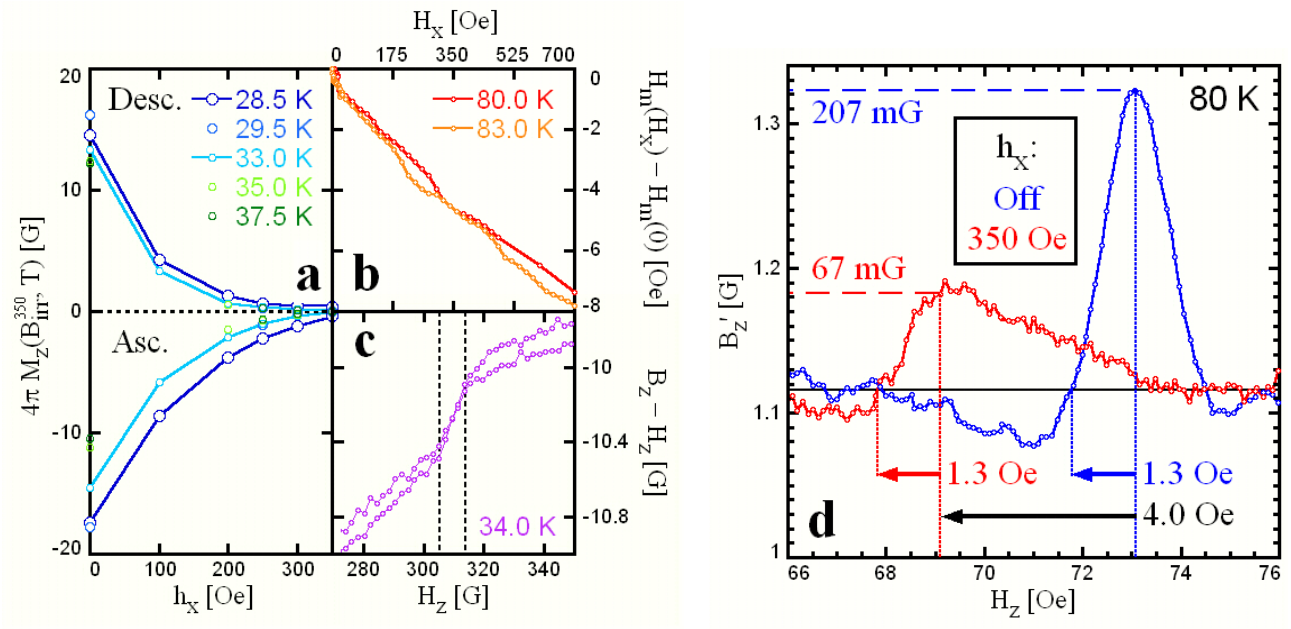

Fig. 4.2: *The effects an in-plane field has on the PV matter, seen with the OPD sample.* (**a**) *Deviation of the magnetization from its equilibrated value at various shaking amplitudes (bottom: ascending sweep, top: descending sweep). The hysteretic magnetization decays with increasing h_x, but so does its slope.* (**b**) *The melting field reduces linearly in the presence of a dc in-plane field.* (**c**) *Result of shaking at 34 K - reversible magnetization showing a broadened first-order melting step.* (**d**) *The broadening as seen in an ac susceptibility measurement at 80 K with the SOD sample. The symmetric melting peak, seen in the absence of a shaking field (blue line), shifted in the presence of a 350 Oe in-plane amplitude (red line) by $\alpha h_x \approx 4$ Oe to lower fields (black arrow), attenuated by $2h_z/(\alpha h_x + 2h_z) \approx 2.5$ (dashed lines), and the high field side of the δ-like peak was replaced by a continuously decaying behavior.*

$H_m^{H_x} = H_m - \alpha|H_x|$ with $\alpha \approx 1.15 \times 10^{-2}$ extracted from the measurement.

Accordingly, an oscillating in-plane shaking field of amplitude h_x results in an oscillating melting behavior

$$H_m^{h_x}(t) = H_m - \alpha|h_x \sin(2\pi f_x t)|. \tag{4.1}$$

Because *dc* measurements perform short integration in time (in our setup the Kithley 182 *dc* voltmeter integrates over 100 ms in each measurement, which is exactly the period of a single shaking cycle $1/f_x = 100$ ms), a sharp thermodynamic phase transition appears as a melting region $\overline{\mathrm{H}}_m = (H_m - \alpha h_x, H_m)$ in such a measurement. The underlying discontinuous melting step ΔB appears to build up gradually along it, where its value at each point $H_z \in \overline{\mathrm{H}}_m$ is weighted by the relative time the induction shows the melted value $H_z > H_m^{h_x}(t)$ within a full

in-plane period, resulting in

$$B_z(H_z) = H_z + \Delta B \times \begin{cases} 0 & , H_z < H_m - \alpha h_x \\ 1 - \frac{2}{\pi} \arcsin\left(\frac{H_m - H_z}{\alpha h_x}\right) & , H_z \in \overline{\mathrm{H}}_m \\ 1 & , \text{otherwise} \end{cases} . \tag{4.2}$$

A 350 Oe shaking amplitude would turn a first-order sharp step into a 4 Oe wide transition, before accounting for the contribution due to the sensor's finite size. Indeed the equilibrated inverse melting steps, obtained by shaking, seemed to be less sharp than those obtained at elevated temperatures without its aid (see Fig. 4.2-c).

Broadening of the first-order melting step due to the oscillating shaking field was further verified by the *ac* susceptibility measurement, shown in Fig. 4.2-d. In the presence of an in-plane field of high frequency ($f_x = 10$ Hz) relative to the c-axis measuring frequency ($f_z = 1$ Hz) the oscillating value of the melting field (4.1) can again be accounted for by the effectively time averaged melting behavior (4.2), whose derivative

$$\frac{\partial B_z(H_z)}{\partial H_z} = 1 + \begin{cases} \frac{2\Delta B}{\pi} \left[(\alpha h_x)^2 - (H_m - H_z)^2\right]^{-1/2} & , H_z \in \overline{\mathrm{H}}_m \\ 0 & , \text{otherwise} \end{cases} \tag{4.3}$$

is to be convolved, according to (3.5), with the δ-like W_{h_z}, given in (3.6), as to obtain the in-phase melting signature B_z'. Unlike the sharp step, considered in (3.7), the derivative (4.3) of the broadened step has a singularity at $H_m - \alpha h_x$, which sets in discontinuously when approached from below, but decays continuously along $\overline{\mathrm{H}}_m$ above it. Consequently, the output signal B_z' (the result of the convolution operation) is composed of half of the δ-like window W_{h_z} at fields lower than $H_m - \alpha h_x$, and a continuous decay along $\overline{\mathrm{H}}_m$ at higher ones.

In addition, because W_{h_z} is normalized, integration of B_z' over H_z yields the melting step ΔB, a result which remains valid also for the broadened case considered here. It further implies, that broadening of the melting peak is accompanied by its attenuation, as to maintain the area beneath it constant. Approximating the peaks shape as triangular yields an attenuation of the broadened peak's height by $2h_z/(\alpha h_x + 2h_z)$ relative to the nonbroadened symmetric one (inversely proportional to the width ratio of their bases). In Fig. 4.2-d the observed shift of the peak maximum to lower fields and its attenuation in the presence of a shaking field (red line) are shown to fit quantitatively our predictions.

As a consequence of the artificial dynamic broadening, introduced by high shaking fields (especially in view of the reduced efficiency at higher amplitudes, discussed above), we used a default 350 Oe shaking amplitude. Still, sharper results came only when we performed temperature sweeps instead of sweeping the applied field. Using the slope of the melting line $\mathrm{d}H_m/\mathrm{d}T \gtrsim 5$ Oe/K (far enough from T^*) to translate the 5 G wide step, seen along a field

sweep while shaking, results in a predicted 1 K (or less) wide melting step to be seen along a temperature sweep. For the translation to be valid the underlying transition has to be locally sharp, and only artificially broadened by dynamic effects.

We performed such measurements, in which the temperature was swept, while applying a constant c-axis magnetic field and an in-plane shaking field (along the dashed line of Fig. 2.7). A representative outcome of such a sweep is given in Fig. 4.3. Two opposite in sign, equally sharp magnetization steps were clearly resolved both in the descending and the ascending temperature sweeps (marked by blue and red lines respectively). Each step in the descending sweep occurs 0.2 K higher than its counterpart in the ascending sweep. This tiny hysteresis is attributed to a small temperature gradient between the thermometer and the sample, as a quasi-static temperature sweeping method was used.

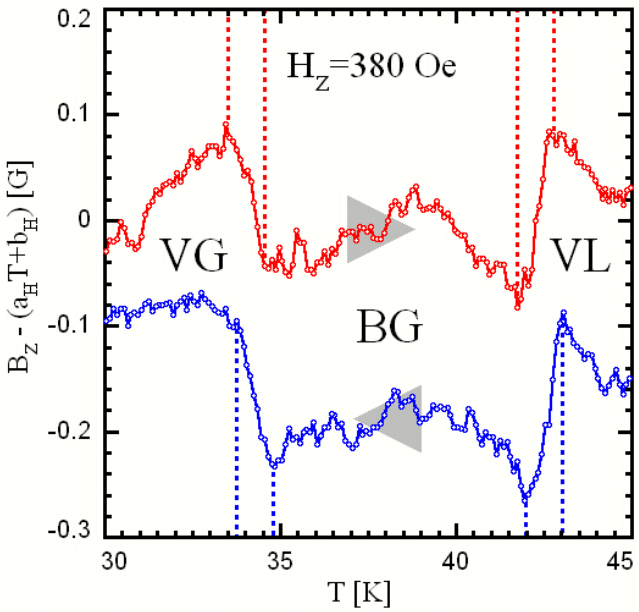

Fig. 4.3: *dc magnetization measurement, taken along a temperature sweep with the SOD sample. Shown is the deviation from a fitted linear dependence of the local induction on temperature. Two equally sharp (dashed lines) melting steps with opposite signs are seen both in a downward (blue line) and an upward (red line) sweeps, marking a gain, followed by a loss, of quasi-long range order along a single sweep.*

The rare thermodynamic scenario of a liquid-solid-liquid sequence, seen within a single reversible temperature sweep, is of course a hallmark of the high temperature thermal melting turning into a low temperature inverse melting behavior, brought about by the disordering pinning potential. The fact, that the two discontinuities attained exactly the same predicted ∼1 K width (emphasized by the dashed lines in Fig. 4.3), is of great importance. It implies, that those mechanisms, which are responsible for the broadening of the well established first-order thermal melting (either time averaging in the presence of shaking or finiteness of sensors), suffice in accounting for the broadening of the step across the inverse melting transition. Consequently, the first-order nature of the thermally-induced phase transition may be equally well ascribed to the disorder induced one.

To further probe the nature of the melting behavior we employed the *ac* susceptibility technique. Being a lock-in measurement, it outputs only the components, that oscillate in and

out of phase with the applied *ac* field, while eliminating the time independent background response to the carrying *dc* field. It is thus crucial, that the *ac* signal would not be screened by pinning or geometrical and surface barriers, and that the vortex matter will have the ability to accommodate to it within each cycle. Obviously, the vortex matter fails to do so as the temperature is lowered. As a consequence, the past use of *ac* susceptibility measurements for the study of the thermodynamics of the vortex matter was restricted to elevated temperatures only (not lower than 70 K).

Within the present study we tried to achieve the relaxation rates, required by the *ac* susceptibility measurement to probe low temperature thermodynamics, by combining it with the shaking method. As both techniques utilize oscillatory magnetic fields (in perpendicular directions), the relation between the two frequencies, f_x (shaking) and f_z (ac susceptibility), was found to have crucial implications, as shown in Fig. 4.4 for two temperatures. Fig. 4.4-a describes the behavior at 45 K, which lies in the thermally driven part of the melting line, while Fig. 4.4-b shows the behavior at 35 K just below T^* within the disorder driven part. Both give the in-phase signal B'_z (properly normalized by the excitation amplitude h_z) versus the swept dc field H_z.

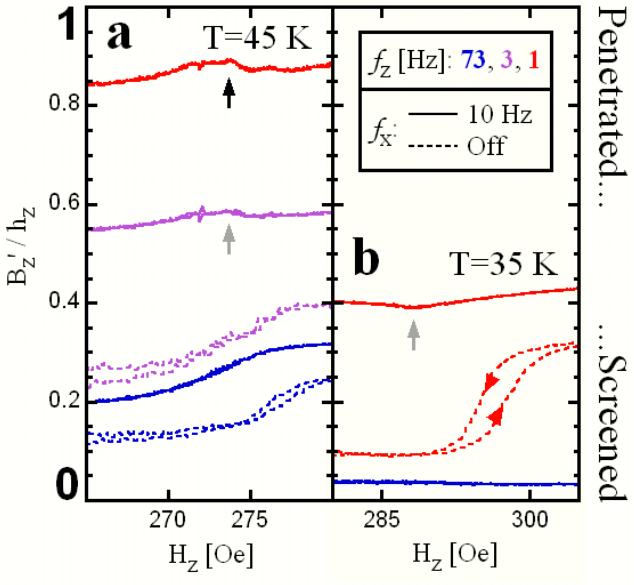

Fig. 4.4: *Incorporation of the ac susceptibility measurement with the shaking method at low temperatures taken in an OPD sample. (**a**) At 45 K ($> T^*$) the screened signal in the absence of shaking (dashed lines) remains screened, when shaking is carried out at high frequency $f_z > f_x$ (solid blue line). As the c-axis frequency is lowered $f_z < f_x$, the penetration improves (solid purple and red lines), and an equilibrium paramagnetic melting peak appears (arrows). (**b**) This behavior repeats itself at 35 K ($< T^*$), except that the partially equilibrated signal (solid red line) shows a diamagnetic melting peak (arrow), the origin of which is not understood.*

The $f_x - f_z$ parameter space can be divided into three distinct regimes, characterized by their low temperature dynamics:

1. $f_x = 0$ (dashed lines) - Fully hysteretic response - The standard *ac* susceptibility measurement. A shaking field is absent, therefore both the response to the *dc* carrier field is hysteretic, marked by the lateral shift between ascending and descending sweeps, and so is the response to the *ac* excitation, marked by the attenuated (screened) signal $B'_z \ll h_z$, picked

by the sensor. An underlying phase transition is marked by the dynamic signature of a slightly increased penetration of the external excitation above the transition.

2. $f_x < f_z$ (solid blue lines) - Fully equilibrated *dc* response with a fully screened *ac* response - The result of a naive simultaneous application of the two techniques. The slow shaking field manages to relax the response to the *dc* carrier field, as seen in Fig. 4.4-a by the reversible behavior between ascending and descending sweeps, but does not enable the vortex matter to follow the *ac* excitation, seen especially by the fully screened signal $B'_z = 0$ (at pickup level) in Fig. 4.4-b.

3. $f_x > f_z$ (solid purple and red lines) - Fully equilibrated *dc* response with at least partially (if not fully) equilibrated *ac* response - Enables probing of low temperature thermodynamics. At 45 K a frequency ratio of $f_x/f_z = 10$ practically recovered a fully equilibrated oscillatory response $B'_z \approx h_z$ (solid red line in Fig. 4.4-a). Accordingly, the dynamic melting signature is replaced by a thermodynamic (somewhat distorted) δ-like paramagnetic peak (black arrow) manifesting a first-order transition. At the same temperature a smaller frequency ratio of $f_x/f_z = 3.3$ resulted in a partially equilibrated (partially screened) response, yet the melting signature is already of the known thermodynamic nature (gray arrow). At 35 K the ratio of $f_x/f_z = 10$ resulted only in partial equilibration of the *ac* response (solid red line in Fig. 4.4-b). The resulting in-phase melting signature was a negative diamagnetic peak (gray arrow).

The dramatic deference between the last two frequency regimes is a direct evidence for the local and instantaneous nature underlying the shaking mechanism. The equilibrated behavior at low temperatures was obtained, only when several shaking h_x cycles could take place within each period of the external h_z excitation. Unfortunately, the experimental setup did not allow us to examine more extreme frequency ratios. We thus conducted all low-temperature *ac* susceptibility measurements with a c-axis measuring frequency of 1 Hz in the presence of a 10 Hz shaking field.

Currently we are not able to resolve the origin of the diamagnetic melting peaks, seen along the inverse melting line ($T < T^*$) with the *ac* susceptibility measurement, as they clearly differ both from the dynamic reduced screening, observed without the use of shaking, and the equilibrated paramagnetic δ-like melting signatures. The fact, that at 45 K a partially equilibrated response did show a thermodynamic signature, may support a thermodynamic origin. On the other hand an equilibrium diamagnetic melting peak can only originate from a first-order melting step, whose sign is opposite to the one, clearly seen in the *dc* magnetization measurements (see Fig. 4.3).

Due to this unresolved ambiguity the nature of the low temperature phase transition can not be inferred from *ac* susceptibility measurements. Still, it can be used in mapping the *B-T* phase diagram of the vortex matter, together with the *dc* magnetization measurements taken along field and temperature sweeps.

4.2 First-Order Melting Transition

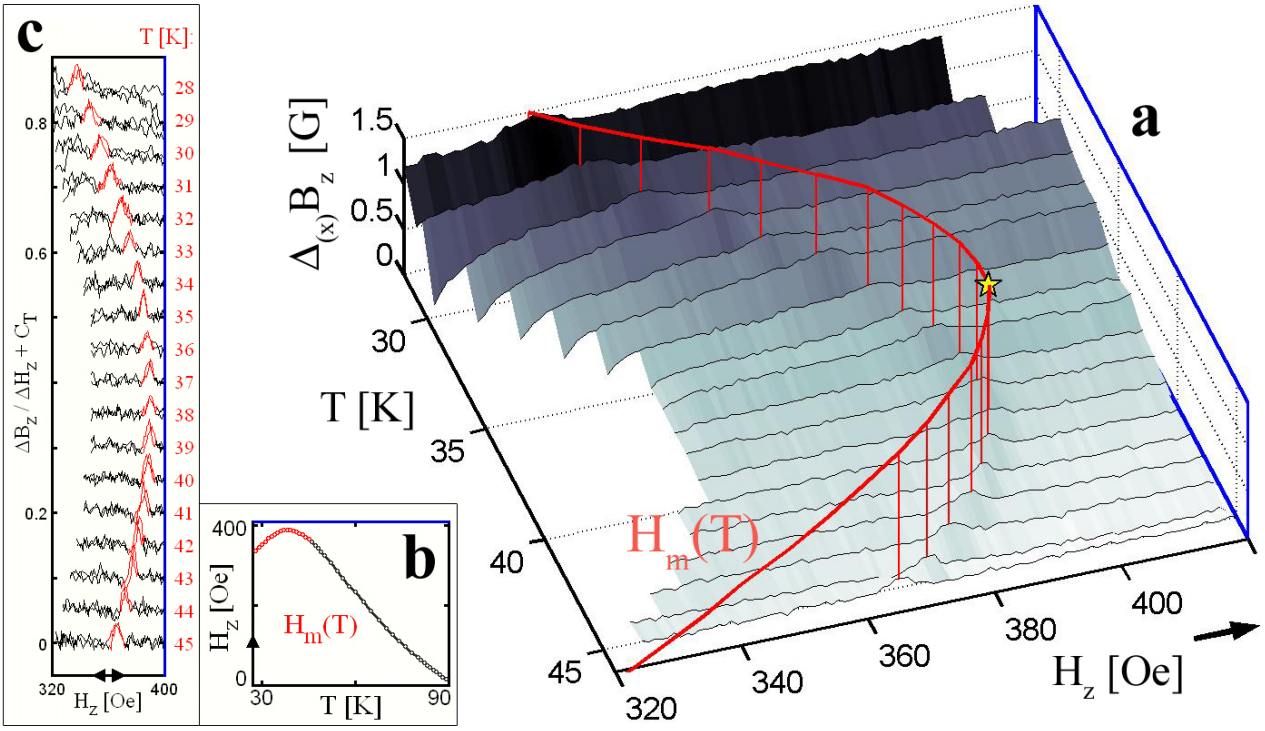

Fig. 4.5: *Melting line $H_m(T)$ of the PV matter as seen in the SOD BSCCO sample, mapped via repeated field swept dc magnetization measurements with shaking. (**a**) Focus on the low temperature melting behavior. Plotted is the difference between two adjacent sensors $\Delta_{(x)}B_z$ versus swept field H_z at various temperatures 28-45 K. Melting is manifested by the small peaks, marked by the vertical red lines. The red curve that interpolates them is the mapped melting line, which changes its slope from positive (inverse melting) to negative at $T^* \approx 39$ K (star). (**b**) The resulting melting line, showing the high temperature thermal melting (negative slope), and low temperature disorder induced inverse melting (positive slope). (**c**) A derivative of the measured induction with respect to the applied field (shifted apart for clarity) shows perfect reversibility of the melting peak feature (red segments) in the presence of the shaking field down to 28K (both ascending and descending sweeps are plotted at each temperature).*

We applied the shaking method in conjugation with all three measuring techniques (field and temperature sweeps of *dc* magnetization measurements and field swept *ac* susceptibility measurement) repeatedly in order to map the *B-T* phase diagram of the PV matter in BSCCO,

and in particular its low temperature thermodynamics, previously obscured by the onset of hysteresis. Cross mapping utilizing all three techniques was done with the prism shaped SOD sample. The profile of the screening currents in such a geometry is symmetric to flux entry and exit, therefore geometrical barriers do not induce a hysteretic magnetization [58]. On the other hand, the slanted surfaces of this geometry together with the layered structure result in a stair-like profile on a microscopic level, that distributes the surface barriers across the sample, and enhances their hysteretic effect [60].

The reversible magnetization, mapped by successive field swept *dc* magnetization loops in the presence of a default 350 Oe - 10 Hz shaking field (applied at all sweeps taken below 60 K), is given in Fig. 4.5. The resulting perfectly reversible behavior (at melting conditions) stretches down to 28 K, as seen in Fig. 4.5-c. It plots the numerical derivative of the local induction with respect to applied field $\mathrm{d}B_z/\mathrm{d}H_z$ versus both ascending and descending applied fields at various temperatures in the range 28-45 K. The results from all temperatures, originally centered around $\mathrm{d}B_z/\mathrm{d}H_z = 1$, were shifted by $C_T = 0.04T - 2.12$ for clarity. The melting peaks (a numerical mimic of the ones, obtained directly with the *ac* susceptibility technique) of the ascending and descending sweeps fall exactly on top of each other, marking loss of memory, which is a mandatory property of an equilibrium state.

The difference between the induction, measured by two adjacent sensors $\Delta_{(x)}B_z$ along the ascending sweep at various temperatures, is given in Fig. 4.5-a. Due to the spatial inhomogeneity, $\partial H_z/\partial x \neq 0$, the vortex matter melts at slightly different applied fields across the sample. In that sense substraction of the induction, as measured by neighboring local sensors, is equivalent to its derivative with respect to applied field (given by Fig. 4.5-c). In addition it eliminates contributions to the local induction, whose origin is not local (the effect of the latter is actually small in the case of equilibrium). Accordingly, melting is signaled by a narrow peak, marked by the vertical red lines. The red curve interpolating between these lines, is the mapped melting peaks, given by Fig. 4.5-b up to its termination at $T_c \approx 90$ K. Its slope changed from positive at temperatures below $T^* \approx 39$ K (yellow star) to negative above it, marking the change in its character from the low temperature disorder driven inverse melting to the high temperature thermally induced transition.

As was demonstrated above (see Fig. 4.3), *dc* magnetization measurements along temperature sweeps in the presence of a shaking field showed reversible magnetization with sharp melting features. Within this study we managed to sample for the first time the thermodynamics of the PV matter also along such sweeps. Fig. 4.6 and its inset give the deviation of the induction from a linear behavior $a_H T + b_H$ (fitted separately for each loop), measured along the descending temperature sweeps at various constant applied fields. $b_H \approx H_z$ is just the background induction $B_z \approx H_z$, while the positive a_H is a small correction to it, which gets con-

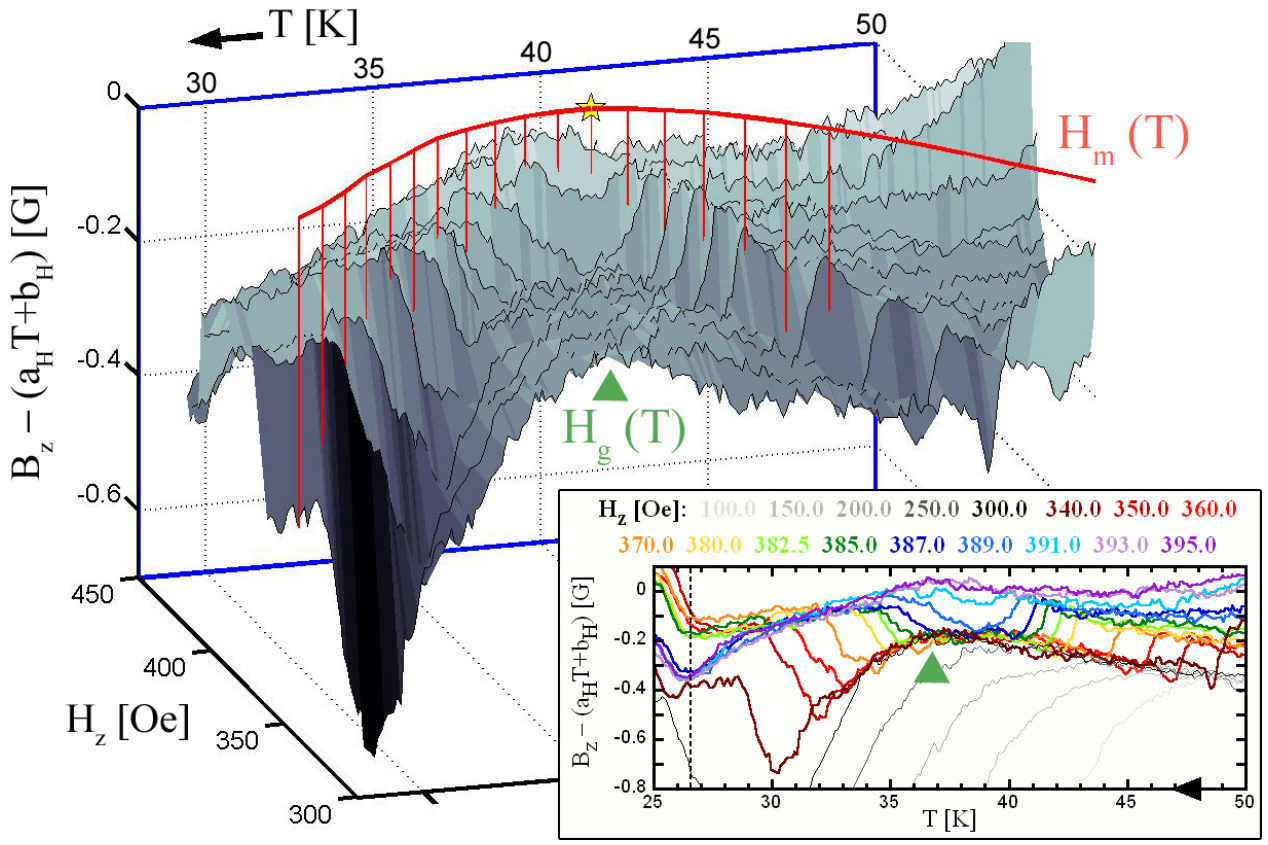

Fig. 4.6: *Equilibrium local magnetization, measured with the SOD sample along temperature sweeps at various applied fields in the presence of a shaking field. Plotted is the deviation of the induction B_z from a linear behavior $a_H T + b_H$. The green triangles mark the narrow temperature region at which the slopes of the magnetization curves changed abruptly. The sharp melting steps follow closely the melting curve (the red curve interpolating between the sampled temperatures), separately measured via field sweeps, advocating a state of equilibrium.* ***Inset:*** *Reversibility was achieved by the shaking field down to ∼26.5 K (dashed line), below which the magnetization became independent of temperature at all applied fields. Consequently, at fields below $H_m(26.5\ K)$ ≈300 Oe (gray-scale lines) only the high temperature melting step was observed.*

tributions both from the vortex thermodynamics and the weak dependence of the Hall constant R_{Hall} on temperature. As a result two unambiguous first-order phase transitions are clearly resolved within each sweep, conducted at fields below $H_m(T^*) = 390$ Oe and above ∼300 Oe.

The red vertical lines in Fig. 4.6 are the same melting points, extracted from the field swept measurements of Fig. 4.5-a, and the red line connecting them is the extracted melting curve. As the field is lowered from 390 Oe the two first-order steps grow apart, following closely the inverse and thermal parts of the unified melting line. The fact, that separate field and temperature sweeps yield identical melting behavior in the presence of a transverse oscillatory field (especially the low temperature part of it, previously obscured by hysteresis) proves, that the ability of the

shaking method to relax the PV matter is not restricted to specific sweeping directions (namely field sweeps), but rather extends to all possible paths within the $B-T$ parameters space, as all paths can be decomposed into reversible segments of field and temperature sweeps.

Local induction became independent of temperature below ~26.5 K, which is marked by the dashed line in the inset to Fig. 4.6 (at least down to 20 K, where the temperature sweeps terminated), at all applied fields. This was, apparently, due to the strong pinning potential at low temperatures, that traps the PVs even in the presence of a shaking field, and consequently 'freezes' the induction profile. The melting line could only be mapped down to this temperature, because below it the melting step was obscured by dynamics, as given by the gray-scale lines of Fig. 4.5-b (the high temperature step was still detected along those sweeps).

Prior to the use of the shaking method in conjugation with *dc* magnetization measurements the melting step ΔB was found to disappear abruptly at T^* [30], which led to the identification of it with a thermodynamic critical point. Below that temperature magnetization measurements showed the second peak feature. Application of the shaking method revealed, that both phenomena are actually the result of irreversibility obscuring the underlying thermodynamics. It is evident from Fig. 4.5-a, b, that the reversible low temperature behavior consists of a first-order melting transition, manifested by a magnetization step ΔB, that retains a finite value at all temperatures, including T^*, which rules out the classification of it as a critical point.

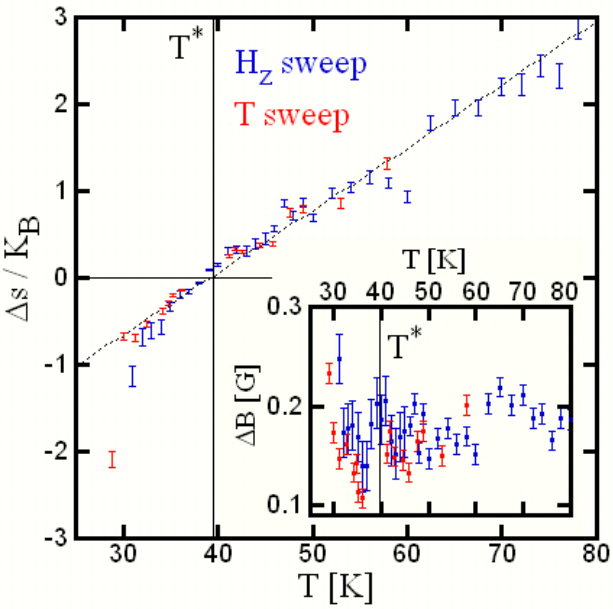

Fig. 4.7: *Temperature dependence of the entropy difference Δs per PV per K_B along the PV melting line, extracted via (4.4) from the magnetization steps ΔB, measured along field and temperature sweeps (blue and red respectively) with the SOD sample. The data of the different sweeping methods agree with each other and fit well an increasing linear behavior (dashed line) both above and below T^* (solid cross).* ***Inset****: Raw $\Delta B(T)$ data.*

The dependence of the melting steps on temperature $\Delta B(T)$, and the implications they bare on the entropy differences between the various phases, are given in Fig. 4.7. The extracted data from field sweep measurements (blue), agrees with that obtained from the temperature sweeps (red). The Clausius-Clapeyron equation (3.1) relates between ΔB and the entropy difference per unit volume ΔS of the phases, involved in the transition,

therefore it enables us to calculate the entropy change per PV

$$\Delta s = -\frac{d\Phi_\circ}{4\pi B_m}\,\frac{\mathrm{d}H_m}{\mathrm{d}T}\,\Delta B, \tag{4.4}$$

which is the quantity given in Fig. 4.7, where the raw ΔB values are given in the inset. In the calculation we have used $d = 15$ Å for the inter-layer spacing, and the extracted local melting induction $B_m(T)$ in the derivative $\mathrm{d}H_m/\mathrm{d}T$, because far enough from H_{c1} the measured local induction $B_z \approx H_z$ gives a better estimation of the locally applied conditions than the externally applied field [61].

The immediate consequence of the thermal melting behavior turning into an inverse melting (while ΔB remains positive) is to make the entropy difference Δs vanish at the melting line's maximum T^*, and turn negative at lower temperatures (as seen in Fig. 4.7), setting T^* itself to be a Kauzmann point ($\Delta B \neq 0$ while $\Delta s = 0$). The negative values, that Δs takes below T^*, imply a very unusual behavior of the entropy. In this temperature region the disordered VG phase has lower entropy than the BrG phase with its quasi-long range correlations, which are known to frustrate thermal fluctuations in the usual case. The inverse melting behavior is a hallmark of a reversed situation, in which pinning destroys quasi-long range order by inducing static dislocations, but at the same time restrains the thermal fluctuations more effectively than the elastic caging forces.

Within the experimental resolution, the entropy difference Δs showed a linear dependence on temperature (dashed line), given by $\Delta s(T) = 2.85 K_B(T/T^* - 1)$ with T^*=39.6 K. The linear behavior was previously observed down to T^* [30]. The present study suggests, however, that the same linear behavior extends also to the low temperature region, reinforcing the view, that nothing critical happens at T^*. Only the lowest resolved magnetization step of each sweeping method deviated significantly from the linear behavior, which may hint on a dynamic origin. Nevertheless, the observed linearly decreasing Δs with decreasing temperatures must reach an extremum and begin to increase at some temperature (lower than the lowest made accessible to us experimentally by shaking), as to obey the third law of thermodynamics itself, that implies $\Delta s(T \to 0) = 0$. This constraint can be satisfied (continuously) either by a vanishing magnetization step (a critical point) or by a vanishing slope of the melting curve somewhere below T^*. The latter is the more common theoretic prediction [41, 49] due to the reduced role of thermal energy relative to elasticity and pinning at low temperatures. Indeed the melting lines, measured from two other samples with higher oxygen doping levels (discussed in the next section), seemed to saturate towards a temperature independent behavior just before irreversibility was met (see orange and green lines in Fig. 4.8).

4.3 Dependence of the First-Order Melting Transition on Oxygen Doping

As discussed within the theoretical background, oxygen contents affects the material anisotropy ε (2.9) turning it more isotropic with increasing doping levels [21]. Anisotropy, in turn, has a fundamental role in setting the properties of the PV matter, as it scales all the characteristic lengthes of the problem. In particular it affects thermal fluctuations and those imposed by disorder, as captured by $Gi(\varepsilon)$ and $\gamma(\varepsilon)$ respectively, where both generally increase with increasing anisotropy, but may still show different dependence on it [2]. Accordingly, the relative role of the different energy scales, involved in the melting process, can be studied by varying the doping levels.

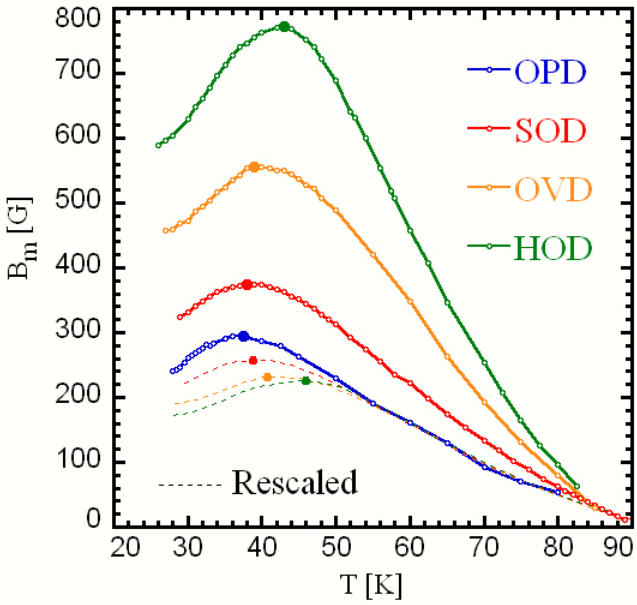

Fig. 4.8: *Equilibrium first-order melting behavior (solid lines) measured with OPD, SOD, OVD and HOD BSCCO samples ($\varepsilon^{-1} \approx 130, 108, 84, 70$ respectively) in the presence of a shaking field. The unified melting curves shift to higher fields with increasing doping, signaling a reduced anisotropy. The inverse melting part becomes more pronounced, and T^* (filled circles) slightly increases. Rescaling the over doped high temperature melting behavior (dashed lines) onto the optimally doped one accounts for the suppressed thermal fluctuations but not for the pinning induced ones.*

We mapped the first-order melting behavior of four BSCCO samples with oxygen content varying from optimally to highly over doped by sampling them along field swept *dc* magnetization measurements, while applying a shaking field at temperatures below 60 K with a 350 Oe amplitude and a 10 Hz frequency. The mapped first-order melting curves of all four samples are given by the solid lines of Fig. 4.8 in terms of the locally measured induction, which gives a more accurate measure of the locally applied field than the externally applied value, versus temperature.

Increase in oxygen concentrations indeed resulted in a shift of the unified melting line (inverse as well as thermal) to higher fields (higher vortex densities), implying reduced thermal and disorder-induced fluctuations with increasing doping levels. T^* (full circles) showed only a mild shift towards higher temperatures. On the other hand, the inverse melting part just

below it became more pronounced and steep, ranging over 200 G in the HOD sample relative to 50 G in the OPD one.

The dashed lines in Fig. 4.8 are the outcome of rescaling the melting curves of the three over-doped samples. Over doping slightly decreases the critical temperature (from 92 K to 86 K when going from the OPD to the HOD sample), therefore we first normalized the temperature scales. We then rescaled the magnetic induction, such that the thermal melting part of the various melting curves will follow the OPD one. The residual dependence on anisotropy is restricted to the low temperature disorder-induced part of the melting curve. The behavior is similar to the one, obtained by increasing the pinning strength alone (e.g by weak electron irradiation [39]). Both result in an unchanged high temperature melting behavior, while the inverse melting part sets in at lower fields and higher temperatures. This suggests, that although reducing anisotropy suppresses both thermal and disorder-induced fluctuations, the former is more affected by it than the latter, therefore depends more strongly on anisotropy ε. A natural explanation for the distinct scaling behavior is that the additional oxygen atoms serve as randomly distributed point-like pinning centers, that enhance the pinning potential, and therefore affect predominantly the low temperature disorder driven phase transition, on top of reducing the material anisotropy.

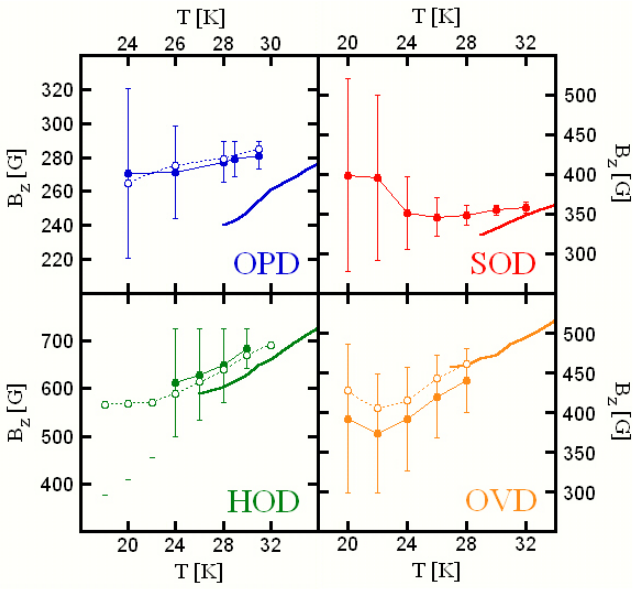

Fig. 4.9: *The low temperature tips of the melting curves (thick solid lines) compared with the dynamical second-peak melting signature. The filled circles connected by thin solid lines are the averages of the onset (upper bar) and offset (lower bar) fields of the second-peak feature, extracted from the descending part of the sweeps (demonstrated by the upper and lower red circles respectively in Fig. 2.8). The open circles connected by dotted lines mark the inflection point.*

In addition, we were able to translate the scaling factors into anisotropy values ε, by knowing how the melting line is predicted to scale with anisotropy (and that $\varepsilon^{-1} \approx 130$ in an OPD material [21]). A model, that accounts only for elastic and thermal energies was sufficient, because rescaling was performed according to the high temperature melting behavior, which is negligibly affected by disorder. We have thus used a Lindemann based result [40], that

yields $B_m(T \gg T^*) \propto \varepsilon^2$, and found $\varepsilon^{-1} \approx 108, 84, 70$ for the SOD, OVD and HOD samples respectively.

We further tried to utilize the scaling behavior, that anisotropy has on the measured thermodynamics, in assessing to what accuracy can the dynamic second-peak feature be used to map the equilibrium melting behavior, as revealed by the shaking method. Fig. 4.9 plots the low temperature inverse melting behavior of the four samples with various doping levels onto their B-T phase diagrams, through the equilibrium melting step, detected in the presence of a shaking field (thick lines), as well as the non-equilibrium second-peak. Because of its dynamic nature, the latter builds up gradually within the field sweep. Accordingly we extracted several possible candidates of signaling the true underlying thermodynamics. Still, the main conclusion is that the second-peak, being a dynamical feature, depends strongly on the properties of the measured sample (its geometry, defects, homogeneity...), on the measurement parameters (sweeping rate, the locally measured position) and not only on the underlying thermodynamics. Nevertheless, out of the various possible lines the one, extracted from the inflection points, generally seems to yield the most reliable result, and to improve with increasing doping levels (these thumb rules are only suggestive, as a larger statistics should be gathered). Note, however, that the second magnetization peak is usually measured by global magnetization, which is expected to give significantly larger deviations from the real thermodynamic melting line.

4.4 Reversible Transition Underlying the Irreversibility Line

We conclude with a new finding, obtained with the temperature swept *dc* magnetization measurements in the presence of a shaking field. The reported observation is preliminary, and should be followed by a more detailed study, especially in view of the implications it bares on the thermodynamics of the PV matter (in particular the BrG phase) as understood to date. The results of the field swept *ac* susceptibility measurements are also presented in this context, as they seem to (at least partially) support it.

We observed an additional sharp and reversible feature in the local induction. At a certain temperature, usually about 37 K, an abrupt change of slope was identified at sweeps taken above as well as below the first-order melting line. It is demonstrated in Fig. 4.10 by the two representative temperature sweeps taken at 420 and 350 Oe (along the pale and dark blue arrows respectively), whose results are quoted at the inset. The measured magnetization was reversible, and the kink in it appeared at the same temperature both on ascending and descending sweeps, as marked by the dashed green lines. The mapping of it at applied fields ranging between 150 and 600 Oe is given in Fig. 4.10 by the solid green line. It crosses the melting curve $H_m(T)$, given in red, at 37 K in close proximity to T^*. This feature showed a

weak field dependence at fields higher than 300 Oe, as seen at the inset to Fig. 4.6, where it is marked by a green triangle, while at lower fields (gray-scale lines) it began to shift towards higher temperatures.

In view of the quasi-static temperature sweeping method we emphasize, that the monitored sweeping rate was nearly constant throughout the measurement and particularly at the vicinity of the observed behavior. It was also robust to deliberate changes of the sweeping rate, hence the change of slope is not an experimental artifact of that sort. Being a sharp transition rules out also the option of it originating from the HSA.

The locus of the mapped feature, as given by the green line in Fig. 4.10, suggests that the B-T phase diagram of the PV matter consists of an additional line $H_g(T)$ along which a second-order phase transition occurs, that intersects the first-order unified melting curve $H_m(T)$ (red line) close to its maximum at T^*. Accordingly, the B-T phase diagram consists of four distinct thermodynamic phases.

The upper part of this line, that lies above the first-order melting transition, fits qualitatively earlier measurements, that mapped the onset of hysteresis due to bulk pinning [71]. The latter was typically found to terminate once it intersected with the melting line in close proximity to T^*, which led to its identification with a thermal depinning or glass melting line, separating the two high field disordered phases [38, 40, 42, 49]. Unlike these experiments, which probed the dynamics (hysteresis) of the PV matter, the present study gives a first evidence for the existence of this line under equilibrium conditions, brought about by the shaking method. It implies on a reversible thermodynamic transition underlying the bulk irreversibility

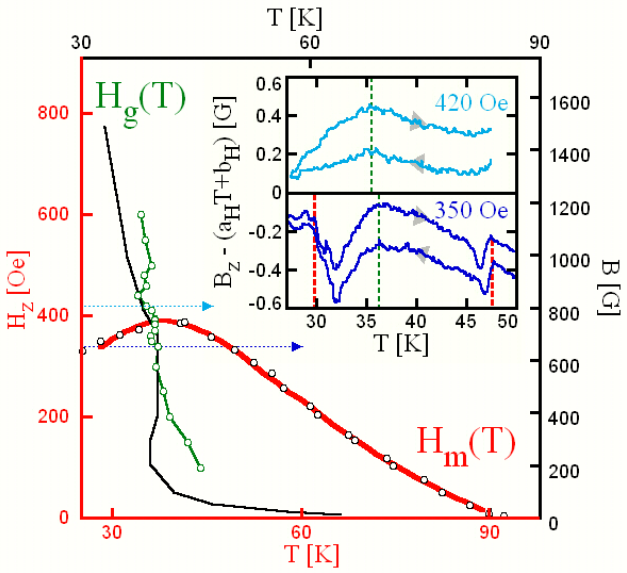

Fig. 4.10: *The mapped B-T phase diagram of the PV matter. The red axes refer to the melting $H_m(T)$ and depinning $H_g(T)$ curves (red and green lines respectively), measured with the SOD sample by temperature wept dc magnetization measurements in the presence of a shaking field. The black axes refer to the dynamic features (black open circles and line respectively), quoted from Ref. [72]. The melting curves were matched to enable the comparison of the depinning lines, which qualitatively agree. Accordingly the phase diagram consists of four distinct phases.* ***Inset****: Two particular temperature sweeps (along the arrows) while applying a 420 Oe and a 350 Oe (pale and dark blue respectively) fields. Both the melting steps and the depinning kinks (red and green dashed lines) were reversible.*

line, setting the low temperature VG and high temperature VL to be two distinct phases (as apposed to the alternative kinetic view of a single phase undergoing a gradual dynamical cross over to a glassy state below some temperature).

In contrast, the continuation of the depinning line into the low temperature BrG region of the B-T phase diagram was very rarely observed by probing of the PV dynamics [72, 73]. One such observation, taken from Ref. [72], is presented in Fig. 4.10 by the black symbols. It was measured by a lock-in transport technique, where the depinning feature (black solid line) was dynamically signaled by the complete screening of the *ac* current excitation from the interior of the sample. To enable a qualitative comparison of the depinning lines, despite the different oxygen doping levels of the two samples, the mapped melting lines (black open circles and red solid line) were matched. As a result the weak temperature dependence, the intersection point with the melting curve and the bending towards higher temperatures at lower fields characteristics seemed to agree between the thermodynamic line (green) and the dynamic one (black), suggesting that the former describes the thermodynamics underlying the dynamics given by the latter. If so, the fact, that both T^* and the intersection point with the melting curve shift together with changing doping levels, suggests that the physics underlying both has to do with balanced pinning and thermal energies, strongly advocating the thermal depinning scenario [2, 74]. In addition, the weak dependence of the depinning line on applied field may be the outcome of thermal deppining, that occurs on a single vortex basis, hence its apparent continuous behavior just above and below the melting curve (weakly depends on the structure of the pinned and unpinned phases involved).

The splitting of the BrG phase by a depinning line of thermodynamic nature calls, yet again, for a revised model for the low field part of the PV matter's B-T phase diagram, as the BrG can accommodate only one out of the two mapped phases. Candidate models are very few, as the concept of a BrG was by itself a very delicate compromise between disorder and quasi long-range order, still we quote two. A recent theoretic study made by B. Rosenstein *et al.* [51] identifies the novel line as a glass transition of the third-order. It restricts the BrG phase to the low field and low temperature portion of the B-T phase diagram, and an unpinned long range-ordered lattice phase is revived to accommodate its high temperatures low field portion. An earlier model, put forward by B. Horovitz [52], offers a more radical change, that gives the Josephson coupling between the PVs a dominant role. It identifies the unified first-order phase transition with a decoupling between PVs in adjacent layers. The high field part of the novel line is also characterized as a depinning transition between low temperature decoupled BrG and high temperature gas (decoupled liquid) of PVs, and the low field phases are two kinds of Josephson glasses of a random inter-layer Josephson coupling induced by disorder, that differ in their coupling strength, where a sharp (although analytic) cross-over line separates them.

An experimental effort should be thus directed beyond the mapping of the borders separating the four phases to supply a better characterization of them (especially the low field ones). Some first dynamical indications of their nature came from the mapping of the B-T phase diagram via the *ac* susceptibility measurements taken also with the SOD sample.

The results are given in Fig. 4.11. It plots the in-phase signal B'_z, picked by the lock-in as a response to the c-axis *ac* excitation of amplitude h_z, along ascending sweeps of the *dc* applied field H_z at various temperatures, while applying a 350 Oe - 10 Hz in-plane shaking field. We compensated for the partial penetration of the external excitation (even in the presence of the shaking field, as discussed in section 4.1) by applying increasing c-axis amplitudes h_z with decreasing temperatures, as to obtain approximately a constant signal within the BrG phase (just before melting occurs) at all sampled temperatures. We set the actual amplitude h_z according to a previously taken set of measurements, which showed an initially slowly decreasing penetration as temperature was lowered from 45 K, and turned more rapid below 37 K. Consequently, we restored a constant signal down to 30 K. Nevertheless, the different penetration regimes may serve as a dynamical evidence of the high temperature phase being indeed less pinned than the low temperature one.

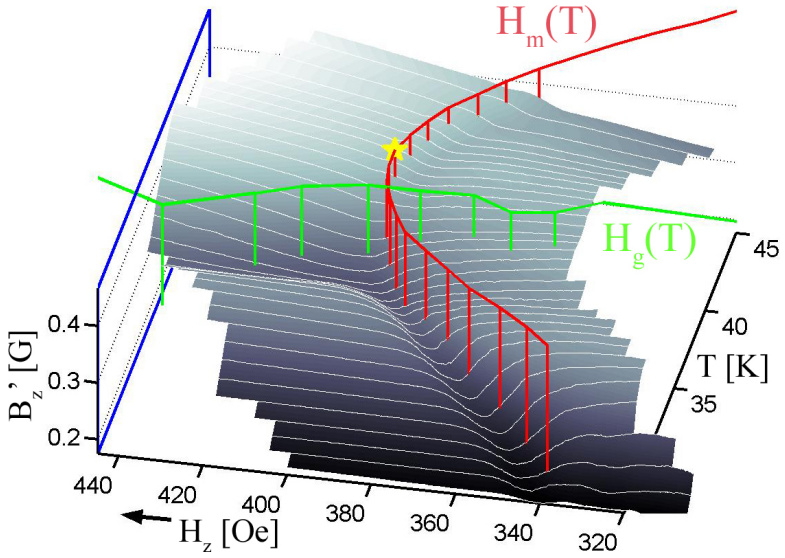

Fig. 4.11: *Mapping of the PV matter B-T phase diagram via field swept ac susceptibility measurements. Both the paramagnetic melting peaks (seen down to 37.5 K) and the diamagnetic ones follow closely the previously measured melting curve (red lines). In addition, both the change in the character of the melting feature and the penetration of the external excitation seem to be affected by the depinning transition (green lines), supporting the depinning scenario.*

The melting feature seemed also to be affected by the depinning transition. The shaking method managed to mobilize the PVs, as to produce an equilibrium melting peak down to 37.5 K. At lower temperatures, on the other hand, the paramagnetic peak was replaced by a small diamagnetic one of a presumably dynamic origin on top of the penetrated *ac* background, as was discussed in section 4.1. Both features followed closely the melting behavior $H_m(T)$ (marked in red), as extracted from the field swept *dc* magnetization measurements (see Fig. 4.5).

The turn over from a thermodynamic feature to a dynamic one took place once the depinning line $H_g(T)$ (green), extracted from the temperature swept *dc* magnetization measurements (see Fig. 4.10), was crossed from its high temperature side. Such a behavior can be attributed to the sharp cross-over into a strongly pinned regime, consistent with the change in the screening of the background, for which we have compensated.

In addition, while the low field $H_z < H_m(T)$ partially penetrated signal showed an artificial temperature independent behavior (which is only the result of our screening compensation scheme), the high field $H_z > H_m(T)$ penetrated signal showed a non-monotonic temperature dependence in the vicinity of the depinning line $H_g(T)$ (green lines), marked by the valley-like feature (which might be as well an artifact of the screening compensation). Below it the external excitation became increasingly screened, while above 39 K the behavior was again temperature independent. Over all, the dynamic screening behavior seems to support a growing effect of pinning on going from the high temperature high field disordered phase clock wise through the two low field relatively ordered phases and towards the high field low temperature disordered phase.

Still, as stated above, both the mapping of the B-T phase diagram and the dynamic characterization of the phases that occupy it call for further research in view of the reported novel phase transition.

5. Summary

The equilibrium B-T phase diagram of the pancake vortex matter in BSCCO was studied through various local magnetization measurements, while making use of the shaking method. Further evidence for the physics underlying the shaking method was also obtained.

We found that an *ac* in-plane field of 350 Oe amplitude and a frequency of 10 Hz manages to reveal the equilibrium melting behavior as seen in local *dc* magnetization measurements down to below 30 K in all four measured samples. Nevertheless, in addition to its relaxation effect on the PV matter, it induces an oscillating behavior in the pancake vortex density, which results in artificial broadening of the originally sharp thermodynamic signatures. Temperature sweeps provided first-order melting steps, that were as sharp for the thermally and disorder induced transitions, strongly supporting the firs-order nature of the inverse melting behavior.

Incorporation of a rapid ($f_x/f_z = 10$) shaking field with the *ac* susceptibility technique enabled its extended use for the mapping of the equilibrium B-T phase diagram down to the cross-over temperature T^* from thermal to inverse melting. At even lower temperatures the partially equilibrated signature was of dynamic nature, which can still provide valuable dynamical indications for the comparative study of the glassy phases.

Cross-mapping by field and temperature swept *dc* magnetization measurements of the unified first-order melting line yielded identical melting behavior, advocating its thermodynamic nature, achieved by the shaking method. The melting steps $\Delta B(T)$, extracted from the two sweeping directions, were also in good agreement. The calculated entropy jump along the melting line was well fitted by a linear behavior above as well as below T^*. The negative values of the entropy jump below T^* imply, that the entropy of the disordered phase is (counter intuitively) lower than that of the quasi-ordered phase.

The pancake vortex melting behavior, as mapped in the over-doped samples, gave conclusive evidence for the unified nature of the melting curve. The inverse melting part of it became much more pronounced with increasing doping levels (decreasing anisotropy). Rescaling of the melting behavior according to the thermally-induced part of the melting line failed to account for the anisotropy effect on the disorder-induced part, suggesting a different anisotropy dependence, or enhancement in the disordering pinning strength with increasing doping levels.

Finally, a novel reversible transition line was detected with the temperature swept *dc* magnetization measurements, which seems to be of second-order. It intersects with the first-order melting line close to T^*, dividing the B-T phase diagram into four distinct thermodynamic phases. Comparison with previous dynamic results suggests, that this line marks a depinning or glass transition, underlying the bulk irreversibility behavior, below which the vortex matter phases are characterized by enhanced pinning.

This last finding calls for a revised characterization of the whole B-T phase diagram of the pancake vortex matter in BSCCO, or at least its low field thermodynamics.

References

[1] G. Bednorz, K.A. Müller, *Z. Phis.* **B64**, 189 (1986).

[2] G. Blatter, M.V. Feigl'man, V.B. Geshkenbein, A.I. Larkin, V.M. Vinokur, *Rev. Mod. Phys.* **66**, 1125 (1994).

[3] N. Avraham *et al.*, *Nature* **411**, 451 (2001).

[4] H.K. Onnes, *Leiden Comm.* **120b**, **122b**, **124c**, (1911).

[5] W. Meissner, R. Ochsenfeld, *Naturwissenschaften* **21**, 787 (1933).

[6] F. London, H. London, *Proc. Roy. Soc.* **A149**, 71 (1935).

[7] J. Bardeen, L.N. Cooper, J.R. Schrieffer, *Phys. Rev.* **108**, 1175 (1957).

[8] V.L. Ginzburg, L.D. Landau, *Zh. Ekzperim. i. Teor. Fiz.* **20**, 1064 (1950).

[9] L.P. Gor'kov, *Zh. Ekzperim. i. Teor. Fiz.* **36**, 1918 (1959).

[10] M. Tinkham, *Introduction to Superconductivity*, McGraw-Hill, Chapter 4 (1996).

[11] A.A. Abrikosov, *Zh. Ekzperim. i. Teor. Fiz.* **32**, 1442 (1957).

[12] U. Essman, H. Träuble, *Phys. Lett.* **24A**, 526 (1967).

[13] D. Criber, B. Jarcot, L. Mdhav, B. Farnoux, *Phys. Lett.* **9**, 106 (1968).

[14] H.W. Weber, J. Scheller, G. Lippman, *Phys. Status Solidi (b)* **57**, 515 (1973).

[15] M. Koyanagi, R.P. Huebener, J. Bosch, R. Gross, *Phys. Rev. Lett.* **54**, 1448 (1985).

[16] T. Matsuda *et al.*, *Phys. Rev. Lett.* **62**, 2519 (1989).

[17] P.H. Kes, A.M. Troyanovski, J. Aarts, *Nature* **399**, 665 (1999).

[18] A.M. Change *et al.*, *Europhys. Lett.* **20**, 645 (1992).

[19] P.E. Goa *et al.*, *Supercond. Sci. Technol.* **14**, 729 (2001).

[20] W.E. Lawrence, S. Doniach, *Low. Temp. Phys.* **16**, 607 (1974).

[21] B. Khaykovich, E. Zeldov, D. Majer, T.W. Li, P.H. Kes, M. Konczykowski, *Phys. Rev. Lett.* **76**, 2555 (1996).

[22] G. Blatter, V.B. Geshkenbein, A.I. Larkin, *Phys. Rev. Lett.* **68**, 875 (1992).

[23] J.R. Clem, *Phys. Rev. B.* **43**, 7837 (1991).

[24] L.N. Bulaevskii, M. Ledvij, V.G. Kogan, *Phys. Rev. B.* **46**, 366 (1992).

[25] A.E. Koshelev, *Phys. Rev. Lett.* **83**, 187 (1999).

[26] E.H. Brandt, *Phil. Mag. B* **80**, 835 (2000).

[27] D.R. Nelson, *Phys. Rev. Lett.* **60**, 1973 (1988).

[28] H. Safar, P.L. Gammel, D.H. Huse, D.J. Bishop, J.P. Rice, *Phys. Rev. Lett.* **69**, 824 (1992).

[29] D.T. Fuchs, E. Zeldov, D. Majer, R.A. Doyle, T. Tamegai, S. Ooi, M. Konczykowski, *Phys. Rev. B.* **54**, R796 (1996).

[30] E. Zeldov, D. Majer, M. Konczykowski, V.B. Geshkenbein, V.M. Vinokur, H. Shtrikman, *Nature* **375**, 373 (1995).

[31] H. Pastoriza, M.F. Goffman, A. Arribere, F. de la Cruz, *Phys. Rev. Lett.* **72**, 2951 (1994).

[32] R.A. Doyle, D. Liney, W.S. Seow, A.M. Campbell, *Phys. Rev. Lett.* **75**, 4520 (1995).

[33] A. Schilling *et al.*, *Nature* **382**, 791 (1996).

[34] R. Cubitt *et al.*, *Nature* **365**, 407 (1993).

[35] S.L. Lee, P. Zimmermann, H. Keller, M. Warden, I.M. Savić, R. Schauwecker, D. Zech, R. Cubitt, E.M. Forgan, P.H. Kes, T.W. Li, A.A. Menovsky, Z. Tarnawski, *Phys. Rev. Lett.* **71**, 3862 (1993).

[36] E.H. Brandt, G.P. Mikitik, *Physica C* **388**, 645 (2003).

[37] A.I. Larkin, *Zh. Ekzperim. i. Teor. Fiz.* **58**, 1466 (1970).

[38] T. Giamarchi, P. Le Doussal, *Phys. Rev. B.* **52**, 1242 (1995).

[39] B. Khaykovich, M. Konczykowski, E. Zeldov, R.A. Doyle, D. Majer, P.H. Kes, T.W. Li, *Phys. Rev. B.* **56**, 517 (1997).

[40] V. Vinokur, B. Khaykovich, E. Zeldov, M. Konczykowski, R.A. Doyle, P.H. Kes, *Physica C* **295**, 209 (1998).

[41] D. Ertas, D.R. Nelson, *Physica C* **272**, 79 (1996).

[42] D.S. Fisher, M.P.A. Fisher, D.A. Huse, *Phys. Rev. B.* **43**, 130 (1991).

[43] M.P.A. Fisher, *Phys. Rev. Lett.* **62**, 1415 (1989).

[44] P. Olsson, S. Teitel, *Phys. Rev. Lett.* **87**, 137001 (2001).

[45] Y. Nonomura, X. Hu, *Phys. Rev. Lett.* **86**, 5140 (2001).

[46] Y. Radzyner, A. Shaulov, Y. Yeshurun, *Phys. Rev. B.* **65**, 100513 (2002).

[47] G.P. Mikitik, E.H. Brandt, *Phys. Rev. B.* **64**, 184514 (2001).

[48] D. Li, B. Rosenstein, *Phys. Rev. Lett.* **90**, 167004 (2003).

[49] J. Kierfeld, V. Vinokur, *Phys. Rev. B.* **69**, 24501 (2004).

[50] P.G. Debnedetti, F.H. Stillinger, *Nature* **410**, 259 (2001).

[51] B. Rosenstein, D. Li (unpublished)

[52] B. Horovitz, R. Goldin, *Phys. Rev. Lett.* **80**, 1734 (1998).

[53] C.P. Bean, *Rev. Mod. Phys.* **36**, 31 (1964).

[54] C.P. Bean, J.D. Livingston, *Phys. Rev. Lett.* **12**, 14 (1964).

[55] E. Zeldov, A.I. Larkin, V.B. Geshkenbein, M. Konczykowski, D. Majer, B. Khaykovich, V.M. Vinokur, H. Shtrikman, *Phys. Rev. Lett.* **73**, 1428 (1994).

[56] T. Schuster, M.V. Indenbom, H. Kuhn, E.H. Brandt, *Phys. Rev. Lett.* **73**, 1424 (1994).

[57] E. Zeldov, D. Majer, M. Konczykowski, A.I. Larkin, V.M. Vinokur, V.B. Geshkenbein, N. Chikumoto, H. Shtrikman, *Europhys. Lett.* **30**, 367 (1995).

[58] D. Majer, E. Zeldov, M. Konczykowski, *Phys. Rev. Lett.* **75**, 1166 (1995).

[59] R.A. Doyle, S.F.W.R. Rycroft, C.D. Dewhurst, E. Zeldov, I. Tsabba, S. Reich, T.B. Doyle, T. Tamegai, S. Ooi, *Physica C* **308**, 123 (1998).

[60] N. Morozov, E. Zeldov, M. Konczykowski, R.A. Doyle, *Physica C* **291**, 113 (1997).

[61] N. Morozov, E. Zeldov, D. Majer, M. Konczykowski, *Phys. Rev. B.* **54**, 3784 (1996).

[62] V.B. Geshkenbein, L.B. Ioffe, A.I. Larkin, *Phys. Rev. B.* **48**, 9917 (1993).

[63] G.P. Mikitik, E.H. Brandt, *Phys. Rev. B.* **69**, 134521 (2004).

[64] M. Willemin, A. Schilling, H. Keller, C. Rossel, J. Hofer, U. Welp, W.K. Kwok, R.J. Olsson, G.B. Crabtree, *Phys. Rev. Lett.* **81**, 4236 (1998).

[65] D.E. Farrell, E. Johnston-Halperin, L. Klein, P. Fournier, A. Kapitulnik, E.M. Forgan, A.I.E. Rae, T.W. Li, M.L. Trawick, R. Sasic, J.C. Garland, *Phys. Rev. B.* **53**, 11807 (1996).

[66] G.K. Perkins, A.D. Caplin, L.F. Cohen (unpublished)

[67] N. Motohira *et al.*, *J. Ceram. Soc. Jpn. Int.* Ed. **97**, 994 (1989).

[68] S. Ooi, T. Shibauchi, T. Tamegai, *Physica C* **302**, 339 (1998).

[69] C.A. Bolle, P.L. Gammel, D.G. Grier, C.A. Murray, D.J. Bishop, D.B. Mitzi, A. Kapitulnik, *Phys. Rev. Lett.* **66**, 112 (1991).

[70] A. Schilling, R.A. Fisher, N.E. Phillips, U. Welp, W.K. Kwok, G.W. Crabtree, *Phys. Rev. Lett.* **25**, 4833 (1997).

[71] R.A. Doyle, B. Khaykovich, M. Konczykowski, E. Zeldov, N. Morozov, D. Majer, P.H. Kes, V. Vinokur, *Physica C* **282**, 323 (1997).

[72] D.T. Fuchs, E. Zeldov, T. Tamegai, S. Ooi, M. Rappaport, H. Shtrikman1, *Phys. Rev. Lett.* **80**, 4971 (1998).

[73] C.D. Dewhurst, R.A. Doyle, *Phys. Rev. B.* **56**, 10832 (1997).

[74] A.I. Larkin, V.M. Vinokur, *Phys. Rev. Lett.* **75**, 4666 (1995).